Master Thesis

Development and Characterization of a Particle Dosing System

carried out at

Institute of Chemical, Environmental and Bioscience Engineering
TU Wien
under the supervision of
Ao.Univ.Prof. Dipl.-Ing. Dr.techn. Michael Harasek
and
Projectass. Dipl.-Ing. Markus Bösenhofer

by

Stefan Tjaden
Matr.Nr.: 00926172

Date

Signature

Acknowledgment

First, I would like to take the chance to thank my parents, my brother and my partner, who made my studies possible.
I would also like to thank Professor Michael Harasek, who gave me the opportunity to work on this thesis at the Institute of Chemical Engineering at Technische Universität Wien.
Special thanks goes out to Projectass. Markus Bösenhofer for his scientific guidance and constant support.
Special appreciations to K1-Met GmbH and project partners: Primetals Technologies GmbH, voestalpine Stahl Linz GmbH, voestalpine Stahl Donawitz GmbH, who made the whole project possible.
Finally, I would like to thank everyone from the research group "Computational Fluid Dynamics (CFD)", especially Eva-Maria Wartha, Thomas Nanz, Christian Jordan and Bahram Haddadi Sisakht for their scientific input.

Abstract

Injection of pulverized coal into the raceway zone of a blast furnace reduces the metallurgical coke consumption and thus, the production cost of pig iron production and CO_2 emissions. Therefore, investigation of pulverized coal conversion in the raceway zone of the blast furnace has become an important research topic for iron and steel manufacturing companies. However, under intense raceway conditions thermo-chemical coal conversion is still under research. The high heating rates and temperatures as well as the elevated pressure, which are predominant in the raceway zone, affect the conversion behavior of the coal particles.

A novel lab-scale test reactor is being developed at Technische Universität Wien for the investigation of pulverized coal conversion. One of many key components is the dosing unit which introduces a solid-gas stream in a controlled manner into the reactor. The aim of this thesis is to develop and characterize a suitable dosing unit for the novel test reactor. The dosing unit should provide a controllable and constant solid-gas injection rate.

A literature review produced two perspective designs of dosing units for the application in the novel test reactor. Both designs were subsequently designed and tested using salt particles as solid and pressurized air as fluid phase. Additional experiments with coal particles and nitrogen were then carried out for one of the dosing units to assess its suitability for application in the novel lab-scale test reactor.

A design of experiment and a statistical analysis revealed potential parameters and their influence on the mass flux for both dosing units. Furthermore, the results enabled the development of models for both dosing units, based on a multiple linear regression, to predict the mass flux. Experimental tests revealed that one of the dosing units is not suitable for the novel lab-scale test reactor, since it is not possible to maintain a solid mass flux in the desired range. For the application as a dosing unit for the novel lab-scale test reactor, however, the design and materials utilized must be optimized to ensure a continuous mass flux for pulverized coal and nitrogen.

Kurzfassung

Einblasen von Kohlestaub in die Racewayzone eines Hochofens reduziert den metallurgischen Koksbedarf pro Tonne Heißmetall und daher auch die Kosten der Eisenproduktion sowie das Emittieren von CO_2. Die Untersuchung von Kohlestaubumsetzungsraten in der Racewayzone eines Hochofens ist ein sehr wichtiges Forschungsthema für Eisen und Stahlfirmen weltweit geworden. Die Auswirkungen der intensiven Racewaybedingungen auf den thermochemischen Kohlenumsatz werden noch erforscht. Die hohen Aufheizraten und Temperaturen sowie der erhöhte Druck, welche in der Racewayzone vorherrschen, beeinflussen das Umsetzungsverhalten von Kohlepartikeln.

Ein neuartiger Testreaktor im Labormaßstab wird auf der Technischen Universität Wien entwickelt um das Umsetzungsverhalten von Kohlestaub zu untersuchen. Eine Schlüsselkomponente stellt dabei die Dosiereinheit dar, welche einen Feststoff-Gas Strom in kontrollierter Form in den Reaktor einbringen soll. Das Ziel dieser Arbeit ist die Entwicklung und Charakterisierung einer geeigneten Dosiereinheit für den neuartiger Testreaktor im Labormaßstab. Die Dosiereinheit soll für einen kontrollierbaren und konstanten Feststoff-Gas Strom sorgen. Weiteres soll ein numerisches Model für diese Dosiereinheit erstellt werden welche den Massenstrom berechnen kann.

Zwei mögliche Dosierkonzepte wurden mithilfe einer Literaturrecherche identifiziert. Zwei Dosiereineiten wurden auf Basis der gefundenen Konzepte entworfen und anschließend mit Salz als Feststoff und Druckluft als Trägergas getestet. Bei einer dieser Dosiereinheiten wurden weitere Versuche mit Staubkohle und Stickstoff durchgeführt um die Eignung für den Einsatz als Dosiereinheit für den neuartiger Testreaktor im Labormaßstab zu untersuchen.

Eine statistische Versuchsplanung gefolgt von einer statistischen Auswertung brachte potentielle Parameter und deren Einfluss auf den resultierenden Massenstrom für beide Dosiereinheiten zum Vorschein. Weiteres ermöglichten die Resultate die Entwicklung von Modellen für beide Dosiereinheiten, basierend auf multiple lineare Regression, um den Massestrom vorauszusagen. Experimentelle Tests ergaben, dass eine der Dosiereinheiten nicht geeignet ist für den neuartiger Testreaktor im Labormaßstab, da der vorausgesetzte Massenstrom Bereich nicht erreicht wird. Für den Einsatz als Dosiereinheit für den neuartiger Testreaktor im Labormaßstab müssen daher erst das Konzept und die verwendeten Materialien optimiert werden um sicher zu gehen, dass ein konstanter Massenstrom für Kohlestaub und Stickstoff realisiert werden kann.

Contents

1 Introduction **1**
1.1 Motivation . . . 1
1.2 Objectives . . . 2

2 Theory **3**
2.1 Gas-Solid Flows . . . 3
2.1.1 Characterization of Particles . . . 3
2.1.2 Minimum Fluidization Velocity . . . 6
2.1.3 Terminal Velocity . . . 8
2.1.4 Characterization of Fluidized Bed Systems . . . 9
2.1.5 Characterization of Pneumatic Transportation Systems 10
2.2 Design of Experiment . . . 12
2.3 Statistics . . . 15
2.3.1 Multiple Linear Regression . . . 15
2.3.2 Analysis of Variance . . . 17

3 Dosing Units **18**
3.1 Vessel Doser . . . 18
3.2 Revolver Doser . . . 19
3.3 Venturi Doser . . . 19
3.4 Mechanical Screw Doser . . . 20

4 Vessel Doser **21**
4.1 Dimensioning . . . 21
4.2 Setup . . . 23
4.3 Trial Conditions . . . 25
4.4 DOE Results . . . 27
4.5 Statistics . . . 30
4.5.1 First Approach . . . 30
4.5.2 Final Approach . . . 33
4.6 Discussion . . . 37

5 Revolver Doser **41**
5.1 Dimensioning . . . 41
5.2 Setup . . . 43
5.3 Trial Conditions . . . 44
5.4 Revolver Doser (RD) DOE Results . . . 46
5.5 Statistics . . . 49
5.5.1 First Approach . . . 49

5.5.2 Final Approach 50
5.6 Vertical Setup 54
5.7 Coal Tests 57
5.8 Discussion 61

6 Conclusion **65**

7 Outlook **67**

A Sieve Analysis 500 μm **i**

B Sieve Analysis 150 μm **v**

C Results of the Vessel Doser (VD) **ix**

D Results of the Revolver Doser (RD) **xiii**

List of Figures

Figure 1 Reducing agents consumption in pig-iron making process 1
Figure 2 Feret and Martin Diameter 3
Figure 3 Geldart classification of particles 5
Figure 4 Correlation of fluid velocity and pressure loss 7
Figure 5 Grace diagram 9
Figure 6 Rabinovich diagram 11
Figure 7 2^3 DOE matrix 12
Figure 8 Schematic illustration of the Vessel Doser concept. . . . 18
Figure 9 Schematic illustration of the Revolver Doser concept. . 19
Figure 10 Schematic illustration of the Venturi Doser concept. . . 20
Figure 11 Schematic illustration of the Mechanical Screw Doser concept. 20
Figure 12 Riser, column and distribution plate of the Vessel Doser (VD) 21
Figure 13 Tee connector of the Vessel Doser (VD) 22
Figure 14 Bottom of Vessel Doser (VD) 22
Figure 15 Schematic of the Vessel Doser (VD) 23
Figure 16 Example trials for the Vessel Doser (VD) 26
Figure 17 Effect plots of the Vessel Doser (VD) 28
Figure 18 Interaction plots of the Vessel Doser (VD) 29
Figure 19 Main effects of the Vessel Doser (VD) 29
Figure 20 Linear Regression of the MLR of the Vessel Doser (VD) - First Approach 30
Figure 21 Linear Regression of the MLR of the Vessel Doser (VD) - Improved Model 31
Figure 22 Linear Regression of the MLR of the Vessel Doser (VD) - Final Approach 33
Figure 23 Normal distribution of residuals for the MLR of the Vessel Doser (VD) 35
Figure 24 Scatter plot of the residuals for MLR of the Vessel Doser (VD) 35
Figure 25 Surface plot of the Vessel Doser (VD) - $\dot{M}$ as a function of $\dot{V}$ and d 37
Figure 26 Surface plot of the Vessel Doser (VD) - $\frac{\dot{M}_s}{\dot{M}_g}$ as a function of $\dot{V}$ and d 38
Figure 27 Surface plot of the Vessel Doser (VD) - $\frac{\dot{V}_s}{\dot{V}_g}$ as a function of $\dot{V}$ and d 39

Figure 28 Characterization of flow regimes for the Vessel Doser (VD) 40
Figure 29 Perforated disc for the Revolver Doser (RD) 42
Figure 30 Schematic of the Revolver Doser (RD) 43
Figure 31 Example trials for the Revolver Doser (RD) 45
Figure 32 Regression of the rotational speed of the disc (RPM) and the mass flux of the Revolver Doser (RD) 47
Figure 33 Effect and interaction plot of the Revolver Doser (RD) 48
Figure 34 Main effects of the Revolver Doser (RD) 48
Figure 35 Linear regression of the MLR of the Revolver Doser (RD) - First Approach 49
Figure 36 Linear regression of the MLR of the Revolver Doser (RD) - Final Approach 50
Figure 37 Normal distribution of residuals for the MLR of the Revolver Doser (RD) 52
Figure 38 Scatter plot of the residuals for the Revolver Doser (RD) 53
Figure 39 Vertical setup of the Revolver Doser (RD) 54
Figure 40 Linear regression of the rotational speeds (RPM) and $\dot{M}$ of the vertical Revolver Doser (RD) setup 56
Figure 41 Wall-effect of coal particles in the Revolver Doser (RD) 58
Figure 42 Two failed coal tests of the Revolver Doser (RD) 59
Figure 43 Regression of the rotational speed of the disc (RPM) and the mass flux of the Revolver Doser (RD) of the coal tests 60
Figure 44 Surface plot of the Revolver Doser (RD) - $\dot{M}$ as a function of RPM and h 61
Figure 45 Surface plot of the Revolver Doser (RD) - $\frac{\dot{M}_s}{\dot{M}_g}$ as a function of RPM and h 62
Figure 46 Surface plot of the Revolver Doser (RD) - $\frac{\dot{V}_s}{\dot{V}_g}$ as a function of RPM and h 62
Figure 47 Characterization of flow regimes for the Revolver Doser (RD) 63

List of Tables

Table 1 DOE matrix of a factor 13
Table 2 Full factorial 2^3 DOE matrix 14
Table 3 Calculation of F-statistic 17
Table 4 2^3 DOE matrix of the Vessel Doser (VD) 26
Table 5 Outcome of the DOE trials for the Vessel Doser (VD) . 27
Table 6 2^3 DOE results of the Vessel Doser (VD) 27
Table 7 F-statistic of the Vessel Doser (VD) - Improved Model . 31
Table 8 Results of the Vessel Doser (VD) - First Approach . . . 32
Table 9 F-statistic of the Vessel Doser (VD) - Final Approach . 34
Table 10 Results of the Vessel Doser (VD) - Final Approach . . . 34
Table 11 Estimated solid mass flux of the Revolver Doser (RD) . 41
Table 12 DOE matrix for the Revolver Doser (RD) 45
Table 13 Outcome of the DOE trials for the Revolver Doser (RD) 46
Table 14 DOE results of the Revolver Doser (RD) 47
Table 15 F-statistic of Revolver Doser (RD) - Final Approach) . . 51
Table 16 Results of the Revolver Doser (RD) - Final Approach . 51
Table 17 Estimated solid mass flux of the vertical Revolver Doser (RD) setup 55
Table 18 Results of the vertical Revolver Doser (RD) setup . . . 55
Table 19 Results of the coal tests of the Revolver Doser (RD) . . 58
Table 20 First sieve analysis of salt i
Table 21 Second sieve analysis of salt ii
Table 22 Third sieve analysis of salt iii
Table 23 First sieve analysis of grounded salt v
Table 24 Second sieve analysis of grounded salt vi
Table 25 Third sieve analysis of grounded salt vii
Table 26 Data used for Vessel Doser (VD) calculations ix
Table 27 Regression results of the Vessel Doser (VD) - First Approach x
Table 28 Regression results of the Vessel Doser (VD) - Improved Model xi
Table 29 Regression results of the Vessel Doser (VD) - Final Approach xii
Table 30 Data used for Revolver Doser (RD) calculations xiii
Table 31 Regression results of the Vessel Doser (RD) - First Approach xiv
Table 32 Regression results of the Vessel Doser (RD) - Final Approach xv

1 Introduction

1.1 Motivation

Injection of alternative reducing agents (ARAs) into the raceway zone of a blast furnaces (BF) is a state-of-the-art operation method in modern pig iron production [1]. This method can significantly reduce the metallurgical coke consumption and thus, reduce the pig iron production cost and CO_2 emissions [2].

Different ARAs were utilized throughout the years to reduce the metallurgical coke consumption. Crude oil and natural gas were mainly used 60 years ago. Nowadays, pulverized coal (PC) has become one of the most important ARA for pig iron production throughout the European Union [3]. Figure 1 depicts the change of the reducing agent consumption over the past 60 years in pig iron production [3]. The metallurgical coke consumption declined to 400 kg/tHM, while the injection of coal increased to 200 kg/tHM.

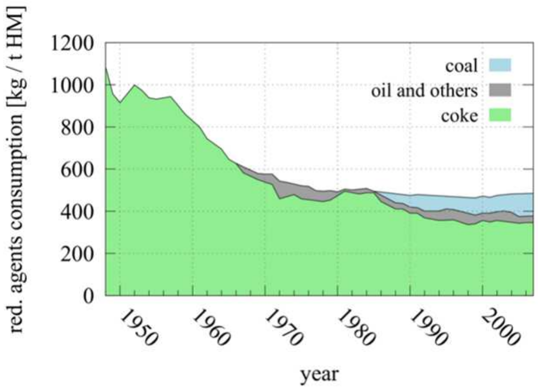

Figure 1: Average consumption of coke, coal, oil and other reducing agents per ton hot metal produced since 1950. [3]

Predicting conversion rates of PC is of high importance, to optimize the pulverized coal injection (PCI) technique. Numerical simulations of the injection process e.g. by Harasek et al. [4] or Zhuo and Shen [5], investigate conversion behavior of pulverized coal in the raceway zone. However, properly acquired experimental conversion rates are of vital importance for these simulations and the evaluation of potential ARAs. To date, no standardized evaluation method has been established for characterization of PC. The biggest problems, for the development of such an evaluation method, are the raceway conditions. The following key parameters for the thermo-chemical coal conversion within the raceway zone of a BF were identified by Babich et al. [6] and Bösenhofer et al. [7]:

- Blast-temperature: 1200 °C
- Heating rate: 10^5 - 10^6 K/s
- Pressure: up to 5 bar
- Gas-particle relative velocity: up to 150 m/s
- Residence time: 20 - 50 ms

Based on available literature, Bösenhofer et al. [7] conclude that there is no reactor which can replicate the intense conditions prevailing in the raceway zone of BFs. Therefore, a novel lab-scale reactor for PC evaluation is planned at the Technische Universität Wien. One of many key components of the novel lab-scale reactor is the particle feeding device. Coal particles are planned to be introduced into the reactor pneumatically via a dosing unit.
In power, pharmaceutical or chemical industry, pneumatic conveying of solids is widely used. Feeding particles into reactors or tanks with a certain mass flux or gas to solid ratio is often the main requirement for such systems. However, pneumatic conveying systems can often pose a challenge for certain applications. Many factors such as the direction of conveying (horizontal or vertical), the particle properties (sizes, shapes, density, etc.) and the utilized carrier gas (density, viscosity, etc.) influence the solid-gas flow significantly [8] [9]. For the development of a feeding device these factors have to be investigated and for the implementation for the lab-scale reactor optimized.

1.2 Objectives

This master thesis focuses on the development of a dosing unit for the feeding of PC into a new lab-scale reactor for PC conversion.
The particle feeding device needs to meet certain requirements to full fill the design criteria of the lab-scale reactor, e.g. mass flow, practicability etc. Maintaining a continuous mass flux with known input is the key for evaluating the resulting conversation rates. In almost the same manner, it is of high importance to be able to set the mass flux to certain gas-solid ratios. The main requirements for the dosing units are:

- Controllable mass flux in the rang of 0.5 - 1.5 g/min
- Continuous mass flux for at least 10 minutes
- Possibility to adjust the gas-solid ratio
- Dosing of pulverized coal with nitrogen

2 Theory

2.1 Gas-Solid Flows

2.1.1 Characterization of Particles

Particles can be characterized according to their physical properties. Two main categories are introduced for the characterization of particles: geometrical and non-geometrical characteristics. Among others, those categories include the following properties:

- Geometrical properties
  - Length
  - Surface
  - Volume
- Non-geometrical properties
  - Mass
  - Density
  - Settling velocity
  - Optical characteristics

The most important geometrical property is a for this thesis is the characteristic particle diameter, which is a length property.

Particle Diameter

The definition of the diameter for non-spherical objects is difficult, since it is strongly dependent on the projection area and contour of the object. Early approaches were realized by introducing the Feret and the Martin diameter. The Feret diameter is defined as the distance between two parallel tangents. The Martin diameter however, is the length of a line, which splits the projected area into two equally sized areas. Figure 2 shows a schematic of the Feret and Martin diameter.

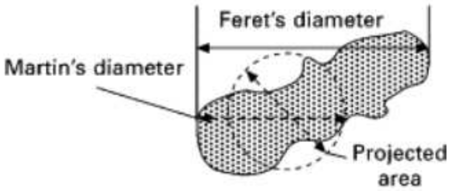

Figure 2: Schematic illustration of the Feret and Martin diameter. [10]

Both were replaced by the equivalent sphere diameter (d_{sv}). [11]. The d_{sv} is calculated by: Equation 1 (where ϕ is a form factor, which is a function of the particle shape and d_p the particle diameter, which is obtained by a sieve analysis).

$$d_{sv} = d_p \cdot \phi \tag{1}$$

The form factor ϕ defines the ratio of the surface area of a particle compared to a volume equivalent sphere. Equation 2 shows the definition of the form factor.

$$\phi = \frac{A_{Sphere}(V_{Particle})}{A_{particle}} \tag{2}$$

Classification

A common approach for characterizing particles for fluidized beds is the "Geldart classification". Particles are classified into four different groups from A to D, according to their fluidization properties. The classification of the particles is based on the d_{sv} and the density difference between the solid and the fluidization fluid. Therefore, each group represents the relation of inter-particle forces (cohesive forces) and hydrodynamic forces between the fluidization fluid and the particles. Figure 3 shows the Geldart [12] classification chart indicating the four groups. [12]

Group A: Particles from this group are suitable for fluidization and pneumatic conveying, since the cohesive forces are negligible.

Group B: Bubbles appear earlier, than for group A particles, when the minimum fluidization velocity is reached for group B particles. Cohesive forces can be neglected for particles in this group.

Group C: Fluidizing group C particles is difficult, since cohesive forces are dominant.

Group D: This group contains solids with high d_{sv}. Similar to group B particles cohesive forces can also be neglected.

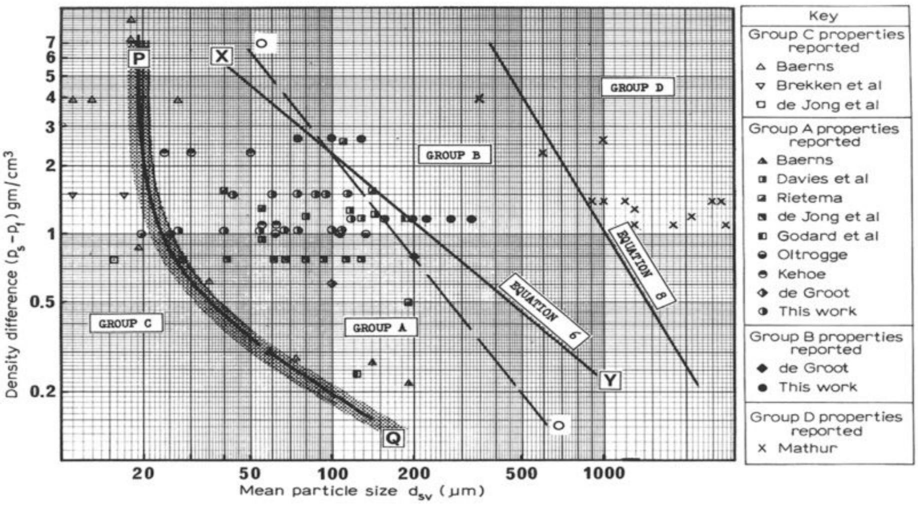

Figure 3: The classification of particles according to Geldart et al. [12].

2.1.2 Minimum Fluidization Velocity

The minimum fluidization velocity (u_{mf}) is described as the minimum velocity the gas or liquid phase has to flow to transit the particles from a packed bed to a fluidized bed. Equation 3 shows the the minimum fluidization velocity (u_{mf}), with the density of the fluid (ρ_f), viscosity of the gas (μ), diameter of the equivalent sphere of the particle (d_{sv}) and the Archimedes number (Ar). [13]

$$u_{mf} = \frac{\mu}{\rho_f \cdot d_{sv}} \cdot [\sqrt{33.7^2 + 0.0408 \cdot Ar} - 33.7] \tag{3}$$

Equation 4 shows the formula of the Archimedes number [14], which is a dimensionless quantity expressing the ratio of the gravitational forces of the particles and the viscous forces.

$$Ar = \frac{\rho_f \cdot d_{sv}^3 \cdot (\rho_s - \rho_f) \cdot g}{\mu^2} \tag{4}$$

The pressure loss in a fluidized bed is constant between the u_{mf} and the terminal velocity u_t. In packed beds, however, the pressure loss depends on the fluid velocity. For laminar flows with a Reynolds number lower than unity, the Carman Kozeny Equation 5 is used [15]. For turbulent flows with Reynolds numbers higher than unity, Ergun [16] added a turbulent component to Equation 5. Equation 6 shows the resulting Ergun Equation. The pressure loss (Δp) in Equation 5 and 6 are calculated with the porosity (ϵ), fluid viscosity (μ), superficial fluid velocity (U), particle diameter (d_{sv}), bed height (H) and fluid density (ρ_f). Beyond u_t the pressure loss rises exponentially and particles are entrained by the fluid.

$$\frac{\Delta p}{H} = 180 \cdot \frac{(1-\epsilon)^2}{\epsilon^3} \frac{\mu \cdot U}{d_{sv}^2} \tag{5}$$

$$\frac{\Delta p}{H} = 150 \cdot \frac{(1-\epsilon)^2}{\epsilon^3} \frac{\mu \cdot U}{d_{sv}^2} + 1.75 \frac{(1-\epsilon)}{\epsilon^3} \cdot \frac{\rho_f \cdot U^2}{d_{sv}} \tag{6}$$

Figure 4 shows the correlation between the fluid velocity and pressure drop of a pneumatic system schematically. The difference between the Ergun and Carman-Kozeny Equation is also indicated.

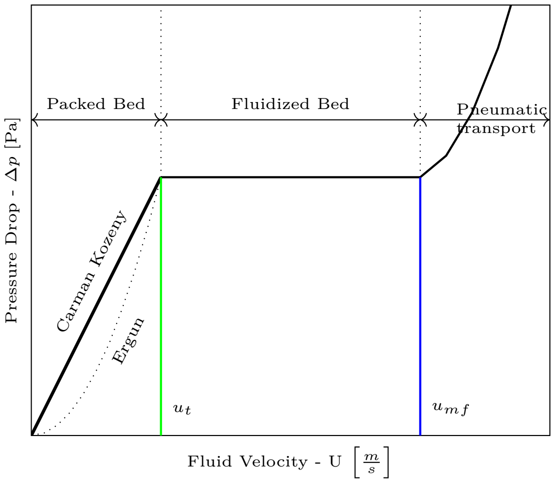

Figure 4: Schematic correlation between the fluid velocity and pressure drop [15, 16].

To maintain an even fluidization, the pressure loss has to be considered during the dimensioning of reactors. The distribution plate underneath the particle bed, needs to have at least 21 % pressure loss compared to the packed bed in industrial sized reactors [17]. Otherwise, the fluid phase is not evenly distributed throughout the packed bed. For experimental equipment with low bed heights the pressure loss has to be much higher in the distribution plate to avoid the so called "Wall-Effect". Tsuji et al. [18] describes the wall-effect as microscopic flows near walls, which prevents the carrier gas from being evenly distributed throughout the packed bed. Therefore, fluidization might not occur even if the u_{mf} is reached.

2.1.3 Terminal Velocity

The terminal velocity (u_t) is the fluid velocity, at which the gravitational force (F_g), seen in Equation 8, is equal to the drag force (F_d), seen in Equation 9 and the lift force (F_l), seen in Equation 10, of a single particle. This force balance can be seen in Equation 7. Surpassing the u_t transitions a system from a fluidized bed to pneumatic transportation.

$$F_g = F_d + F_l \tag{7}$$

$$F_g = m_p \cdot g = \rho_s \cdot V_p \cdot g \tag{8}$$

$$F_d = C_W \cdot A \cdot \frac{\rho_f}{2} \cdot U^2 \tag{9}$$

$$F_l = V_p \cdot \rho_f \cdot g \tag{10}$$

u_t can be expressed with Equation 11 by inserting the Equations 8, 9 and 10 into the force balance (Equation 7), (where m_p is the particle mass, ρ_s the solid density, V_p the volume of the particle, g the gravitational force, A the surface area, ρ_f the density of the fluid and U the superficial fluid velocity).

$$u_t = \sqrt{\frac{4}{3} \cdot \frac{(\rho_s - \rho_f)}{\rho_s} \cdot \frac{g \cdot d}{C_W}} \tag{11}$$

C_W represents the drag coefficient, which is a dimensionless quantity and is a function of the Reynolds number (Re). Equation 12 and Equation 13 show the calculation of C_W and Re.

$$C_W = \frac{24}{Re} + \frac{4}{\sqrt{Re}} + 0.4 \tag{12}$$

$$Re = \frac{\rho_f \cdot u \cdot d_{sv}}{\mu_g} \tag{13}$$

An iterative approach is required to determine C_W, Re and the terminal velocity (u_t).

2.1.4 Characterization of Fluidized Bed Systems

Gas-solid flows in fluidized bed (FB) systems can be described by different approaches. One of the most important characterization is the Grace diagram [19], which characterizes FBs by two dimensionless quantities: the dimensionless velocity (U*) and the dimensionless particle diameter (d*). Equations 14 and 15 show the definition of these quantities.

$$U* = \frac{Re}{Ar^{1/3}} \tag{14}$$

$$d* = Ar^{1/3} \tag{15}$$

Figure 5 shows the Grace diagram including the various FB regimes.

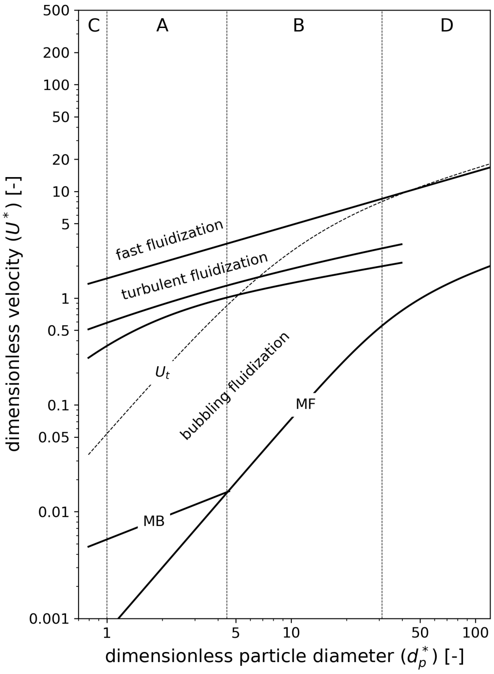

Figure 5: Grace diagram [19] including the different FB regimes. U_t, MF and MB denote terminal velocity, minimum fluidization velocity and minimum bubbling velocity.

2.1.5 Characterization of Pneumatic Transportation Systems

Pneumatic conveying is the transport of solids by a gas stream. Conveying can be divided based on the direction (vertical or horizontal) and in the solid-to-gas ratio (dilute or dense phase) [7]. A solid-to-gas ratio of more than 30 mass ratio is considered as dense phase. This regime type is often preferred in industrial transportation systems, since a dilute phase conveying (lower solid to gas ratio) tends to erode piping systems [8, 9].

Rabinovich and Calman [9] claim that a modified Reynolds number (Re*) and the Archimedes number (Ar) are sufficient to describe vertical conveying systems. Equation 16 shows the modified Reynolds number Re^* which is based on the Reynolds number (Re), the porosity (ϵ) and the solid to total volume flow-rate ratio (c_V).

$$Re^* = Re\left(1 - \frac{\epsilon}{1-\epsilon} \cdot \frac{c_V}{1-c_V}\right) \tag{16}$$

Figure 6 shows the Rabinovich diagram indicating the various flow regimes of vertical pneumatic transport.

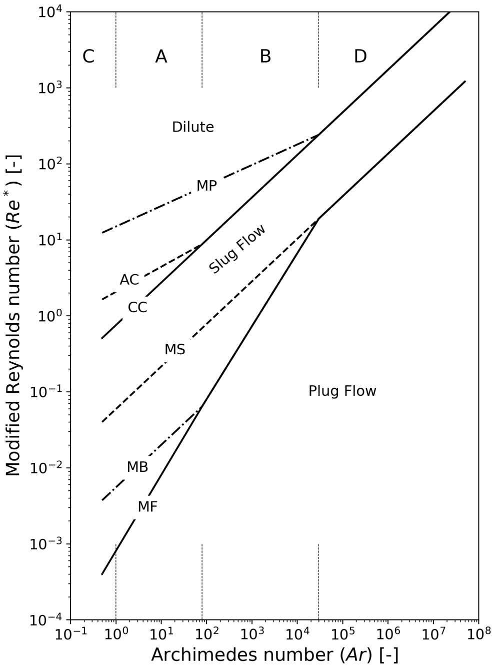

Figure 6: Gas-solid flow regimes described by Rabinovich and Calman [9]. Including U_t, MF, MB, MS, CC, AC, and MP as the terminal velocity, minimum fluidization point, minimum bubbling point, minimum slugging point, classical choking point, accumulated choking point, and minimum pressure point and A,B,C and D the Geldart classification [12].

2.2 Design of Experiment

A design of experiment (DOE) is a systematic approach for the identification of the influencing factors of an investigated system. The initial assumption is always that each process parameter might influence the system's behaviour. Furthermore, a DOE can give valuable insights in the sensitivity of different factors on the system's response, e.g. the solid mass flux of the doser. [20]
For example, a full factorial 2^3 DOE consists of three factors, which are basically input parameters, each having a minimum and a maximum value, also known as settings. Figure 7 illustrates such a 2^3 DOE with three factors (A, B and C) and their settings "-1" and "+1". These settings indicate the high setting (+1) and the low setting (-1). The actual values for the settings are chosen according to the desired range of a factor, since they represent the physical boundaries. Thus, a DOE is an efficient way to characterize experimental systems and their influencing factors. [20]

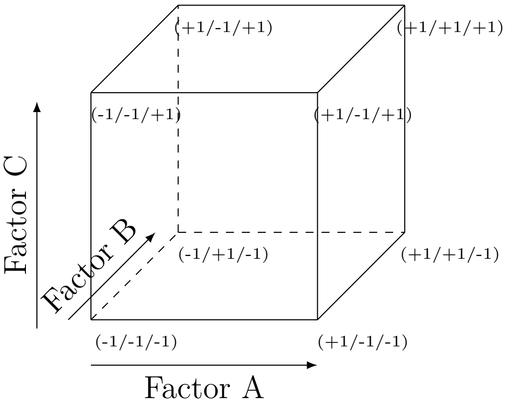

Figure 7: Experimental points for a full factorial 2^3 design of experiment (DOE). The axes A, B and C are 3 different factors with 2 different settings.

The influence of a factor on the system can be characterized by the "Main Effect". The experimental results of a factor with the "-1" settings are subtracted from the results of the "+1" settings, for it's calculation. As a result, the dependence of the system can be observed according to the change in the settings. Table 1 summarizes the DOE matrix of one factor, with two different settings and the corresponding experimental results Y_i. [20]

Table 1: DOE matrix for a factor. Y_i is the output of the system as a result of the different settings "-1" and "+1". The results Y_i of the same settings are averaged to $\bar{Y}_{-1}$ for the "-1" setting and $\bar{Y}_1$ for the "+1" setting.

Settings	Result	Average
-1	Y_1	$\bar{Y}_{-1}$
-1	Y_2	
-1	Y_3	
-1	Y_4	
+1	Y_5	$\bar{Y}_1$
+1	Y_6	
+1	Y_7	
+1	Y_8	

Equation 17 shows the calculation of the main effect.

$$MainEffect = \bar{Y}_1 - \bar{Y}_{-1} \tag{17}$$

To investigate multiple factors and their main effects, each factor has to be included in the DOE matrix. Table 2 shows the DOE matrix for multiple (A, B, C) factors. [20]

Apart from the factors and their main effect onto the experimental result, interactions between two or more factors may occur. For instance factor A and B can interact with each other (AxB) and change the result (Y_i) significantly. To evaluate such an interaction, an interaction effect plot can be used, which indicates the combined behaviour of two factors. In these plots non-interacting factors give parallel lines, while the lines of the interacting factors are non-parallel. [20]

Table 2: Matrix of a 2^3 full factorial DOE. A, B and C being three different factors, each having 2 different settings "-1" and "+1". Y_i is the output of the system for each experiment. AxB, AxC, ... indicate the interaction of 2 or more parameters.

A	B	C	AxB	AxC	BxC	AxBxC	Result
-1	-1	-1	1	1	1	-1	Y_1
-1	-1	1	1	-1	-1	1	Y_2
-1	1	-1	-1	1	-1	1	Y_3
-1	1	1	-1	-1	1	-1	Y_4
1	-1	-1	-1	-1	1	1	Y_5
1	-1	1	-1	1	-1	-1	Y_6
1	1	-1	1	-1	-1	-1	Y_7
1	1	1	1	1	1	1	Y_8

The interaction of two or more factors and their combined influence on a system can also be evaluated using Equation 17. However, the settings for those interacting parameters have to be determined before. This is done by a simple multiplication of the settings of the corresponding parameters. For example the settings of AxB are the result of the multiplication from the settings of the factor A and factor B. Hence "+1" settings results from the multiplication of two "-1" settings or two "+1" settings. [20]

2.3 Statistics

2.3.1 Multiple Linear Regression

Multiple Linear Regression (MLR) is a method to predict a dependent variable $\hat{Y}_i$ from multiple independent variables X_i by estimating correlation coefficients. Equation 18 shows a typical formula for a MLR where ϵ is the error term of the fitted model, also refereed to as the residual. a_i are the coefficients of the independent variables and a_0 is the y-intercept. [21]

$$\hat{Y}_i = a_0 + a_1 \cdot X_1 + a_2 \cdot X_2 + ... + a_n \cdot X_n + \epsilon \tag{18}$$

The aim of a MLR is to establish a model that predict values $\hat{Y}_i$ with a minmal error towards observed values Y_i. The MLR approach relies on the following four key assumptions:

Linear Relationship
A linear correlation between the dependent variables Y_i and the independent variables X_i is the key condition for MLRs. If this condition is not fulfilled a different modelling approach is required. [21]
The linear relationship can be quantified with the coefficient of determination (R^2). Thus, a linear correlation (Equation 19) of the observed dependent variable Y_i and the predicted dependent variable $\hat{Y}_i$ is calculated. R^2 is then expressed through a number between 0 and 1, where 1 indicates a perfect linear correlation. [21]
R^2 is calculated by Equation 22 from the Sum of Squares of the Residuals (SS_{res}) (Equation 20) and the Total Sums of Square (SS_{tot}) (Equation 21). [21]

$$Y_i = k \cdot \hat{Y}_i + d \tag{19}$$

$$SS_{res} = \sum (Y_i - \hat{Y}_i)^2 \tag{20}$$

$$SS_{tot} = \sum (Y_i - \bar{Y})^2 \tag{21}$$

$$R^2 = \frac{SS_{res}}{SS_{tot}} \tag{22}$$

Normal distribution

The difference of Y_i and $\hat{Y}_i$, known as the residuals, have to be normally distributed. If there is no normal distribution of the residuals, a systematic error in the sampling could be the reason. The evaluation of the normal distribution is done visually using histograms or mathematically via the "Kolmogorov-Smirnov test". [21]

Homoscedasticity

In addition to the normal distribution, the residuals should be independent from each other. Meaning that the variance of the error terms should be equal. Evaluation of homoscedasticity can be done by scatter plotting the residuals. The scatter plot reveals, whether the residuals follow a specific, systematically trend or are randomly distributed around the predicted data. [21]

Multicollinearity

A correlation of independent variables should be avoided. In case of a high correlation, those variables have to be combined or excluded from the model. [21]

The Variance Inflation Factor (VIF) [22] is calculated to detect multicollinearity for the independent variables. The VIF is calculated according to Equation 23 using the tolerance defined by Equation 24, which includes R_i^2 the coefficient of determination of a regression of X_i as a function of all other independent variables. A VIF of 1 indicates no correlation between the independent variables. [21]

$$VIF = \frac{1}{tolerance} \tag{23}$$

$$tolerance = 1 - R_i^2 \tag{24}$$

2.3.2 Analysis of Variance

In addition to the MLR, an ANalysis Of VAriance (ANOVA) needs to be applied to verify the viability of the model parameters. In general, the null hypothesis of ANOVA states that the means of multiple groups are equal [23].

To test the hypothesis, the ANOVA uses variances (Equation 25) within groups and compares them to all other tested groups [23].

$$s^2 = \frac{1}{n-1} \cdot \sum (Y_i - \bar{Y})^2 \tag{25}$$

To quantify, whether the means of multiple groups are equal, the F-ratio is calculated from the F-statistic. Table 3 shows the procedure to calculate the F-ratio from the Sum of Squares (SS) and Mean of Squares (MS) from the regression, residual and in total, where k is the number of groups and n the total sample size. [23]

As a result, the F-ratio is expressed by a number above unity, where unity represents a complete equality among the means of the groups. A higher number indicates that the variances within the groups is lower than between the groups. To ensure that the results of the MLR are not by chance, the F-ratio should be as high as possible. [23]

Table 3: Summary of the F-statistic calculation using the degree of Freedom (DF), Sums of Square (SS) and Means of Squares (MS) from the Regression, Residual and in Total. k being the number of factors or "groups" and n the sample size.

	DF	SS	MS	F-ratio
Regression	k	$SS_{reg} = \sum (\hat{Y}_i - \bar{Y})^2$	$MS_{reg} = \frac{SS_{reg}}{k}$	$\frac{MS_{reg}}{MS_{res}}$
Residual	$n-k-1$	$SS_{res} = \sum (Y_i - \hat{Y}_i)^2$	$MS_{res} = \frac{SS_{res}}{n-k-1}$	
Total	$n-1$	$SS_{tot} = \sum (Y_i - \bar{Y})^2$		

Furthermore, the F-ratio is used to estimate the probability-value (p-value) with the help of a "F-distribution table", which is a collection of tables for four different significance levels (α value) of 0.10, 0.05, 0.025 and 0.01 [23]. The p-value is a number which indicates the probability that a certain result is by chance. An α value has to be predefined to determine if a p-value is considered significant. In this thesis the α value is set to 0.05 (5 %). If a group has a higher p-value than 0.05, it is insignificant and therefore rejected. [23]

3 Dosing Units

Kirsch [24] divided the injection of PC into reactors for pyrometallurgical processes at industrial size into two general groups: modified pressure-difference controlled and mechanical-feeder-based controlled.

The basic idea behind modified pressure-difference controlled systems is to fluidize particles within a hopper tank under high pressure and convey the particles in form of a solid-gas mixture through a conveying system. The dosing can be controlled via setting the differential pressure between the hopper tank and the injection point. [24]

In contrary, mechanical controlled feeder introduce particles into a continuous gas stream via a rotary vane or screw system. The dosing can be controlled by the speed of the mechanical screw or vane. [24]

In a literature review the following concepts for lab-scale feeding devices were identified.

3.1 Vessel Doser

Puttinger et al. [25] and Liang et al. [26] utillize a feeding device which fluidizes particles on a porous plate in a vessel and convey the particles pneumatically via a riser out of the vessel. The flow rates of the feeding device can be obtained by continously measuring the weight of the dosing unit. Figure 8 shows a sketch of a Vessel Doser. The carrier gas inlets are situated on the top and on the bottom of the vessel. Particles are stored within the vessel on a porous plate with a riser reaching from the top of the vessel into the packed bed of the particles.

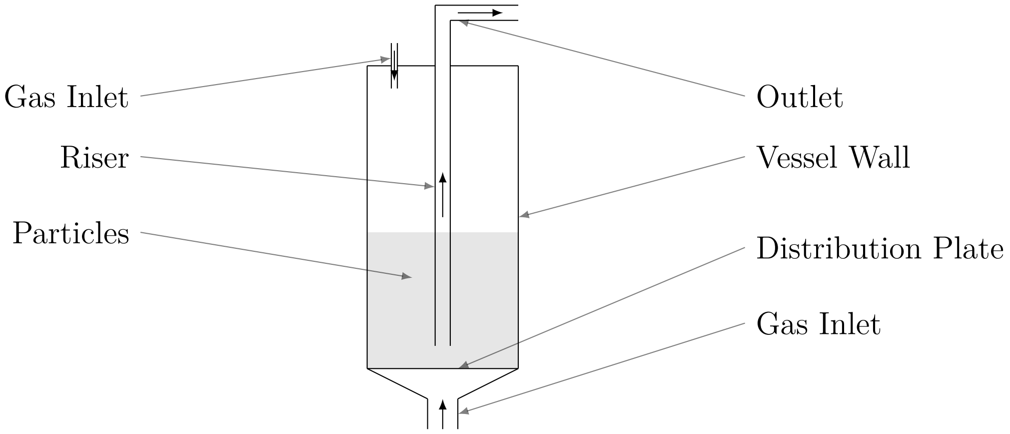

Figure 8: Schematic illustration of the Vessel Doser concept.

3.2 Revolver Doser

Vorobiev [27] describes the feeding of particles via a rotating perforated disc, which transports particles from a fluidized bed towards a slitted pipe with a continuous flow of carrier gas. Particles are picked up by the carrier gas stream on top of the doser and pneumatically conveyed towards the outlet. The mass flux can be controlled with the rotation speed and the design of the rotating perforated disc. Figure 9 shows a sketch of a Revolver Doser. The perforated rotating disc is vertically situated in the middle of the doser. Particles are stored at the bottom, while being fluidized through a porous plate from underneath. The slitted pipe with continuous carrier gas and the outlet is at the top of the doser.

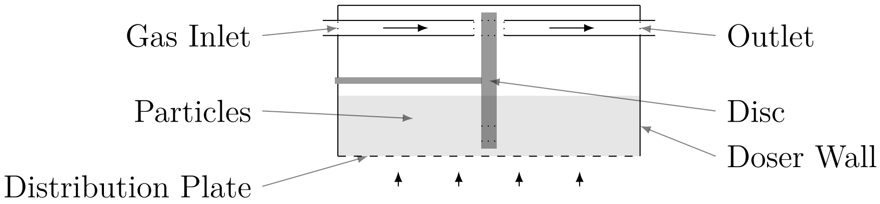

Figure 9: Schematic illustration of the Revolver Doser concept.

3.3 Venturi Doser

Henthorn et al. [28] and Kelly et al. [29] utilize a feeding device which is based on the Venturi effect. Carrier gas passes through a constriction and induce a pressure difference. As a result, particles are sucked out of a hopper tank.

Figure 10 shows a sketch of a Venturi Doser. The inlet of the doser is situated on top of the vessel. Particles are stored within a vessel with a riser reaching from the top into the particle bed. The riser is connected to a constriction with continuous carrier gas stream at the top of the doser.

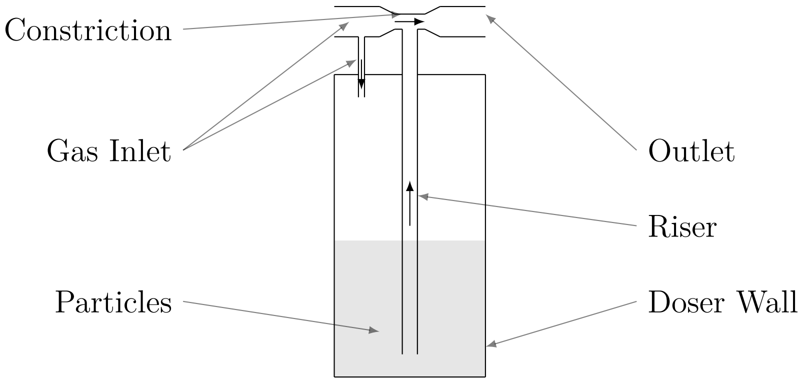

Figure 10: Schematic illustration of the Venturi Doser concept.

3.4 Mechanical Screw Doser

Kirsch et al. [24] describe multiple mechanical feeding devices. One of them is the Mechanical Screw Doser. Particles are introduced into a stream of carrier gas via a vertically rotary screw. Speed and dimensions of the screw control the injected solid mass. Contrary to the previously mentioned Revolver Doser, the particles do not need to be fluidized. Figure 11 shows a sketch of a Mechanical Screw Doser. Particles are stored within a hopper tank. A mechanical screw connects the hopper with a pipe which has a continuous carrier gas stream, where the particles are picked up and conveyed towards the outlet.

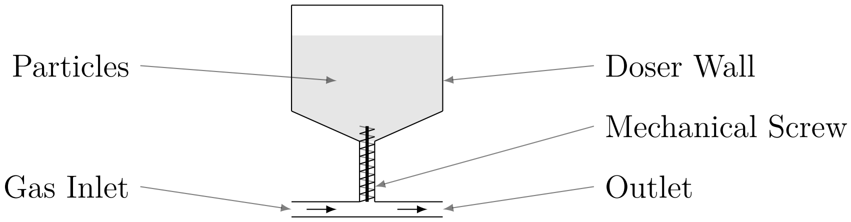

Figure 11: Schematic illustration of the Mechanical Screw Doser concept.

4 Vessel Doser

4.1 Dimensioning

The dimensioning of the Vessel Doser (VD) was a downscaling attempt of an industrial doser [25]. The main requirement was to fit at least 5 kg of salt into the VD and to have a cylindrical column with high particle bed height. This scaling resulted in a cylindrical column with a diameter of 11 cm and a height of 45 cm. The riser in the middle was scaled to a diameter of 11 mm. Figure 12 shows the column including the distribution plate at the bottom. The distribution plate consists of a disc with 20 holes of 1 mm diameter covered with a 100 µm metal mesh.

Figure 12: Picture of the column including the distribution plate and the riser

A tee connector is installed on top of the column. It connects the Streaming Valve (SV), outlet tube and the riser, which is visible in the middle of Figure 12. The column is sealed on the top using a screw joint, sealing ring and a metal plate. In addition, the Column Valve (CV) is installed at the top, which is a gas inlet into the column, at this connection point. Figure 13 depicts the tee connector setup from the side and from the top.

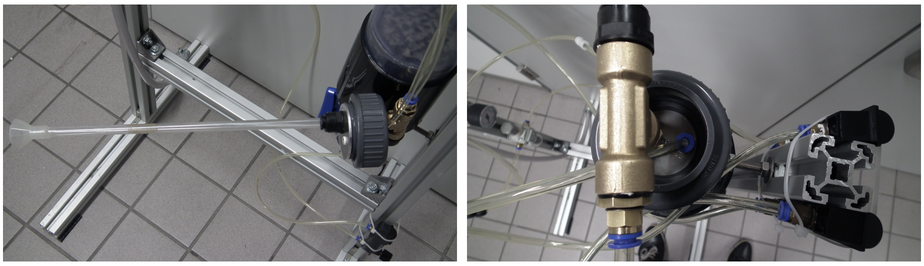

Figure 13: Riser including the screw joint (left). Column Valve (CV) and tee connector for Streaming Valve (SV), outlet tube and riser. (right)

The fluidization valve (FV) is installed underneath the distribution plate as a gas inlet. Figure 14 shows the bottom of the column, including the FV.

Figure 14: Picture of the bottom of the Vessel Doser (VD) column.

4.2 Setup

The particles in the VD are fluidized from the bottom by a gas stream which is controlled by the valve FV. Additional gas can be introduced into the column through the CV. The combined air flow through CV and FV is then forced into the riser and exits the VD through the outlet tube.
Figure 15 depicts a schematic illustration (left) and a picture (right) of the VD. The dismountable riser is installed in the center of the column. The riser needs to be installed for particle conveying. Due to the lower cross-section of the riser compared to the column, the u_t can be surpassed at low volumetric gas flows.

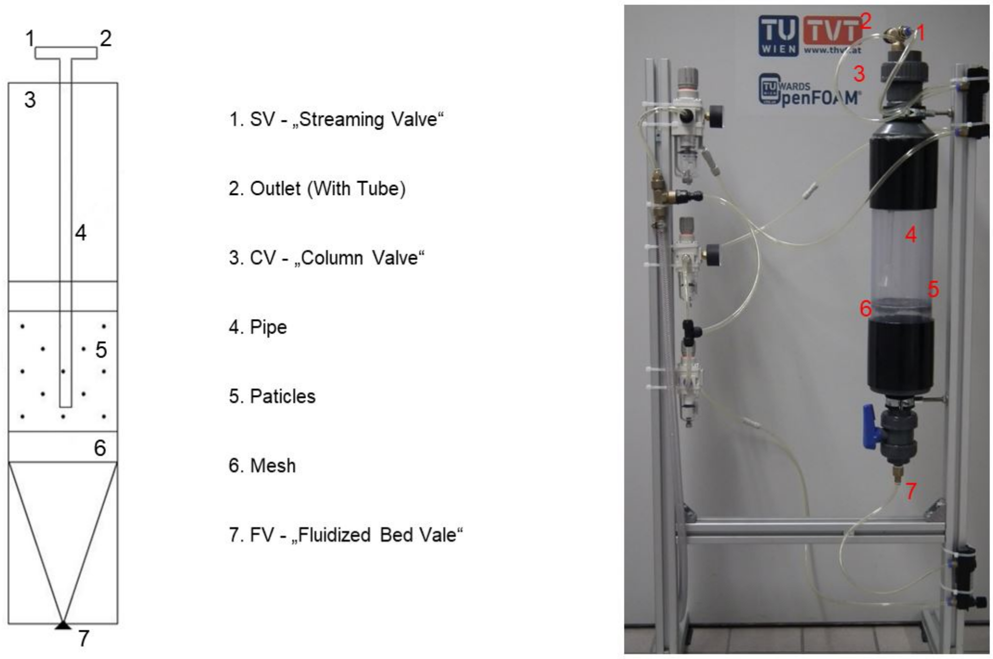

Figure 15: A schematic illustration (left) and a picture (right) of the Vessel Doser (VD).

The VD is filled from the top by removing the screw joint and the pipe. Shutting the screw joint after filling the column with salt has proved to be a challenge, since particles block the riser position. However, it was easy to re-introduce the pipe by fluidizing the particle bed through FV. The timing to shut the screw joint and switch off the volume flow from the FV has to be exact. Otherwise, a significant particle mass is conveyed through the pipe, since the gas velocity is around 100 times higher in the riser than in the column. After filling the VD the outlet tube, having the desired diameter and a length of 1 m, is mounted. This outlet tube is then connected to a collection box equipped with a balance. An integrated mesh on the lid of the box ensured that air could escape while particles were captured. A python script records the balance readings. The flow rates are set manually by adjusting the CV and FV valve through rotameters.

4.3 Trial Conditions

To characterize the VD, three main parameters were considered:

- FV - Volume flow introduced through the "Fluidized Bed Valve"
- CV - Volume flow introduced through the "Column Valve"
- Diameter of the outlet tube

To assess the ranges of the possible total volume flow, u_t and u_{mf} were calculated with the following physical properties:

- Solid phase - Salt (see A)
  - $d_{sv} = 400\ \mu m$
  - $\rho_s = 2160\ kg/m^3$
- Fluid phase - Air
  - $\nu_f = 1.8 \cdot 10^{-6}$ Pa · s
  - $\rho_f = 1.2\ kg/m^3$

The corresponding u_{mf} and u_t are 0.109 m/s and 1.154 m/s. It is necessary to introduce at least 6.6 l/min to reach u_t according to the cross section of the riser (95 mm^2). To reach the u_{mf} within the vessel a gas stream of at least 60 l/min has to be introduced. A range of 8-20 l/min was chosen for the experiments.

For a full factorial 2^3 DOE, the parameters had to be transformed into factors with proper settings to gain as much information in as few experiments as possible. This led to the combination of the FV and CV flow rate to the factors "Total Volume Flow" and "Ratio FV". Furthermore, a high "+1" and a low "-1" setting had to be defined for the DOE. These factors are defined as follows:

- $\dot{V}$ - Total volume flow introduced via FV and CV
  - High - (1): 20 l/min
  - Low - (-1): 8 l/min
- Ratio FV - Ratio of gas introducced via FV vs. CV
  - High - (1): 0.75
  - Low - (-1): 0.25
- d - Diameter of Outlet tube connected to the collection box
  - High - (1): 9 mm
  - Low - (-1): 5 mm

Table 4 shows the 2^3 full factorial DOE. Two repetitions were made for each experiment.

Table 4: DOE experimental setting matrix for the Vessel Doser (VD).

Volume Flow $\dot{V}$ [l/min]	Ratio FV [-]	Diameter [mm]
8	0.25	5
8	0.25	9
8	0.75	5
8	0.75	9
20	0.25	5
20	0.25	9
20	0.75	5
20	0.75	9

Linear regression of the the steady-state experimental region was used to determine the particle mass flow rate. Figure 16 visualizes three example trials. The reason, why the regression was only performed up to 650 g is that trials with lower gas stream were not able to drain the whole column. As a result, other effects than the gas flow rates influenced the solid flow rate e.g. immersion depth of the riser in the particle bed.

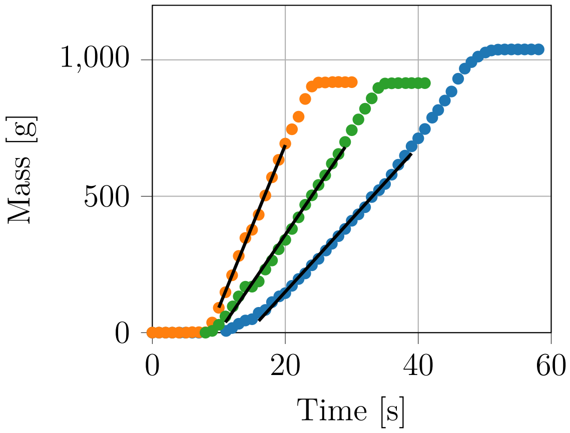

Figure 16: Representative experimental results for the Vessel Doser (VD) including the linear regression of each trial. Blue doted: CV = 15 l/min; FV = 5 l/min; d = 8 mm, orange doted: CV = 5 l/min; FV = 15 l/min; d = 12 mm and green doted: CV = 7 l/min; FV = 7 l/min; d = 10 mm.

4.4 DOE Results

The results of the experiments for each trial are combined into a simple DOE matrix. Table 5 summarizes this DOE matrix, including all factors and the mean mass fluxes for each trial.

Table 5: DOE matrix of the Vessel Doser (VD) including the results.

Volume Flow $\dot{V}$ [l/min]	Ratio FV [-]	Diameter d [mm]	Average [g/s]	Trial 1 [g/s]	Trial 2 [g/s]	Trial 3 [g/s]
8	0.25	5	10.50	11.55	10.29	9.72
8	0.25	9	17.62	14.60	18.97	19.3
8	0.75	5	10.07	10.04	10.33	9.84
8	0.75	9	15.97	14.93	16.85	16.14
20	0.25	5	28.71	30.03	28.91	27.19
20	0.25	9	57.55	60.47	59.60	52.59
20	0.75	5	25.46	23.18	26.70	26.49
20	0.75	9	56.13	54.78	58.46	55.15

Table 6 shows the DOE matrix including the transformed settings ("-1" and "1") of the factors and their interactions.

Table 6: DOE matrix of the Vessel Doser (VD) including the interactions and results.

$\dot{V}$	Ratio FV	d	$\dot{V}$ x Ratio FV	Ratio FV x d	$\dot{V}$ x d	$\dot{V}$ x Ratio FV x d	Avg Mass Flux [g/s]
-1	-1	-1	+1	+1	+1	-1	10.5
-1	-1	+1	+1	-1	-1	+1	17.62
-1	+1	-1	-1	-1	+1	+1	10.07
-1	+1	+1	-1	+1	-1	-1	15.97
+1	-1	-1	-1	+1	-1	+1	28.71
+1	-1	+1	-1	-1	+1	-1	57.55
+1	+1	-1	+1	-1	-1	-1	25.46
+1	+1	+1	+1	+1	+1	+1	56.13

Figure 17 shows the effect plots for the three factors. Increasing the total volume flow ($\dot{V}$) and outlet tube diameter (d) gives higher mass flux rates. In addition, the mass flux rates drop, when the FV/CV ratio is increased.

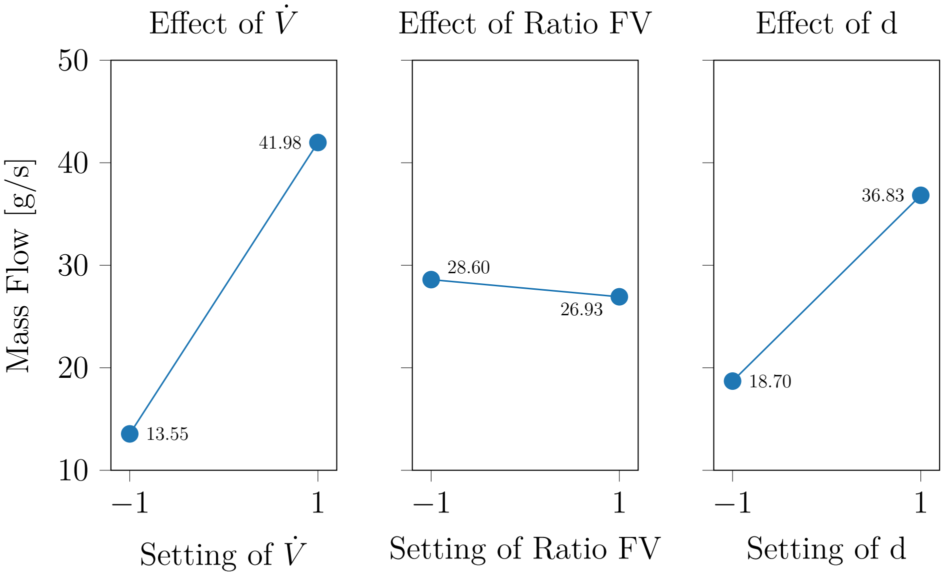

Figure 17: Effect plots of the Vessel Doser (VD) DOE, for each of the three factors: Total volume flow ($\dot{V}$), air ratio introduced through the valves FV/CV (Ratio FV) and outlet tube diameter (d).

Figure 18 shows the interaction plots, which are used to identify co-correlations between the different input factors. $\dot{V}$ and d seem to interact with each other, which is indicated by the non-parallel lines of the high and low settings. On the other hand, the FV/CV ratio does not interact with d or $\dot{V}$, which is indicated by the parallel lines in the interaction plot for high and low settings. Figure 19 shows the main effects of all factors and their possible interactions. According to the results, $\dot{V}$ has the strongest influence on the mass flux, followed by the outlet tube diameter and the interaction $\dot{V}$ x d. The other effects are negligible.

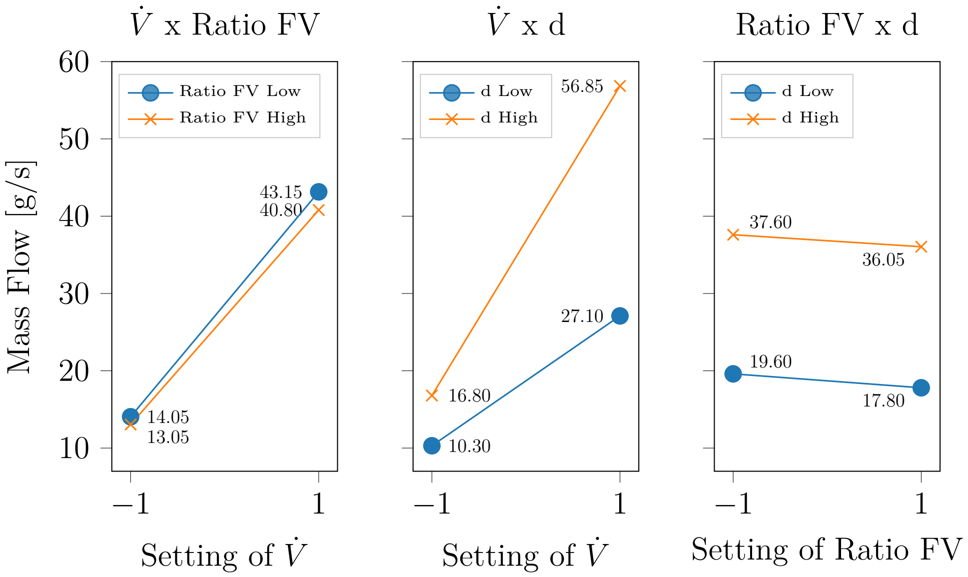

Figure 18: Interaction plots of the Vessel Doser (VD).

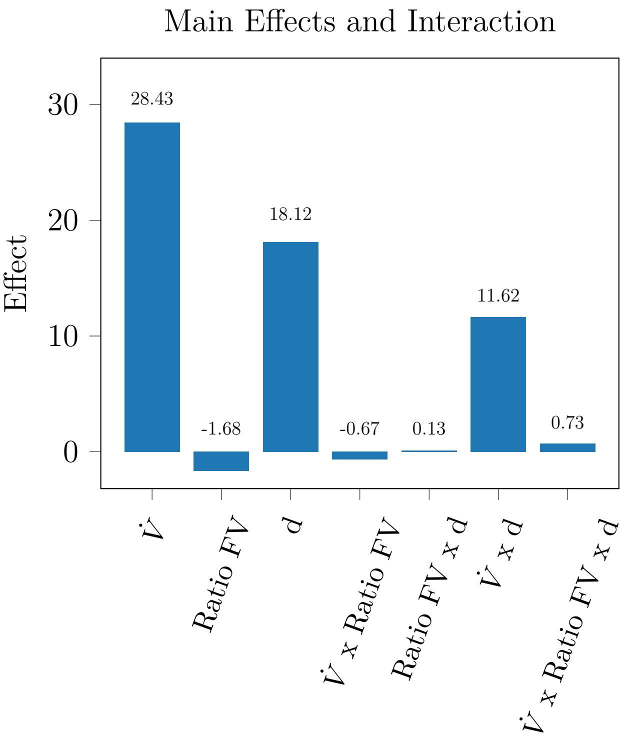

Figure 19: Main effects of all factors and interactions on the solid mass flux of the Vessel Doser (VD).

4.5 Statistics

4.5.1 First Approach

The acquired data summarized in Table 5 was modelled with a MLR and an ANOVA. Figure 20 shows that the predicted values are much higher than the experimental data in the range between 15 and 35 g/min. The R^2 is only 0.8845, which indicates a low quality fit. Therefore, a linear relationship is not given between the predicted values and the experimental data. Subsequently, the fitting procedure was repeated with the logarithmic value of the the solid mass fluxes as the dependent variable. Figure 21 shows the results of this improved model with a quality of fit of $R^2 = 0.9779$.

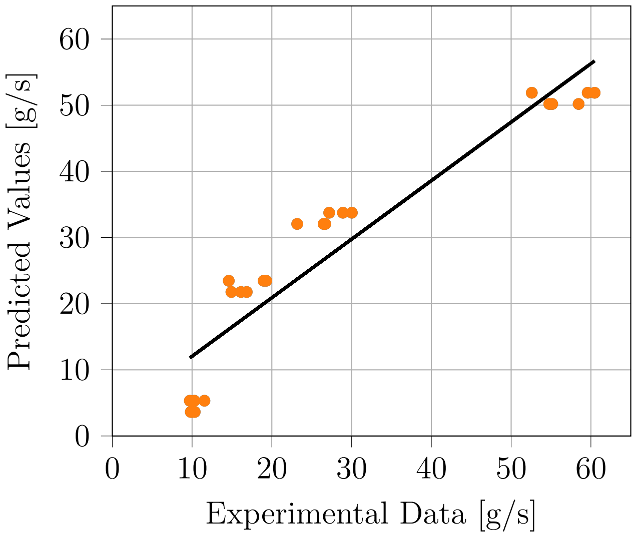

Figure 20: Linear relationship of the predicted values versus the experimental data of the Vessel Doser (VD).

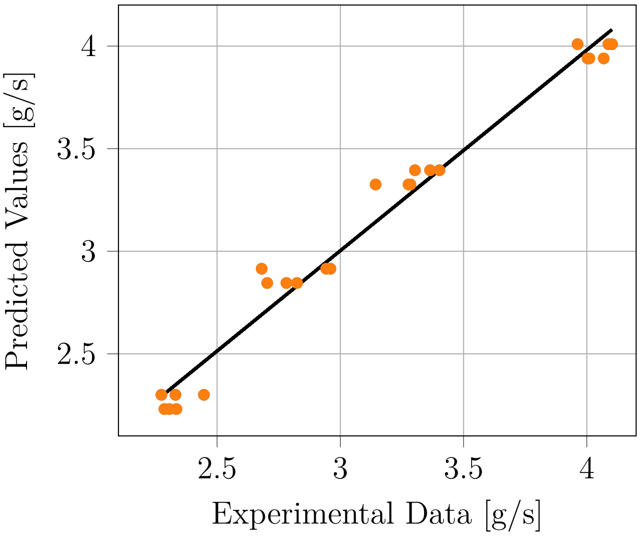

Figure 21: Linear relationship of the predicted solid mass flux versus the experimental data of the Vessel Doser (VD) for the improved model.

The quality of the linear relationship of the improved model can be sumarized with the Standard Deviation of Residuals (SDR) and the R^2:

- SDR: 0,1034
- R^2: 0,9779

Additional statistical parameters need to be reviewed to further evaluate the model quality, as discussed in 2.3.1. The ANOVA results in Table 7 reveal a F-Value of 295.45 which indicates that the results are not caused by random effects.

Table 7: F-statistic of the improved model for the Vessel Doser (VD). DF, SS, MS denote the degree of freedom, sums of squares and means of squares.

	DF	SS	MS	F-Ratio
Regression	3	9.48255	3.16085	295.453
Residual	20	0.21396	0.0107	
Total	23	9.69652		

Table 8 shows the results of the model fitting calculations. The high α value for the variable "Ratio FV" indicates that its influence on the particle mass flux is negligible. The α values for the other influencing parameters are significant, since they are lower than 0.05. These results are in line with the visual interpretation of Figure 17 and the circumstance, that the Ratio FV has no significant influence on the particle mass flux.

Table 8: Regression results of the first approach for the Vessel Doser (VD) including the coefficients, the result of the t-Test and the α values.

Variable	Coefficient ± Std.Err.(coeff)	t-Test	α
INTERCEPT	0.8373 ± 0.1006	8.325	< 0.0001
$\dot{V}$	0.0912 ± 0.0035	25.922	< 0.0001
Ratio FV	-0.1390 ± 0.0844	-1.646	0.1154
d	0.1536 ± 0.0105	14.551	< 0.0001

4.5.2 Final Approach

The preliminary data analysis and model fitting discussed in the previous section suggests that a new MLR model is needed for the present data set, because the effect of Ratio FV is negligible. Therefore, a MLR was modelled. $\dot{V}$ and d were used as independent variables and $ln(\dot{M})$ as dependent variable. Figure 22 confirms a linear relationship between the predicted and measured data for the MLR model, which underlines its applicability.

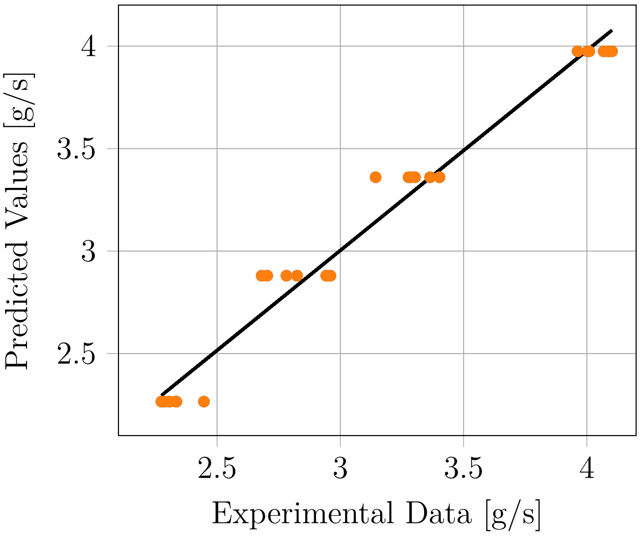

Figure 22: Linear relationship of the predicted values of the new MLR versus the experimental data for the Vessel Doser (VD)

Compared to the previous result, neither the R^2, nor the SDR change significantly. They have the following values for the new MLR:

- SDR: 0.1076
- R^2: 0.9749

Table 9 shows the ANOVA results for the F-statistic and reveal an F-Value of 408.57 which is an improvement compared to the first approach. The calculated α values in Table 10 confirm the significance of both model's variables, $\dot{V}$ and d.

Table 9: F-statistic of the new model for the Vessel Doser (VD). DF, SS, MS denote the degree of freedom, sums of squares and means of squares.

	DF	SS	MS	F-Ratio
Regression	2	9.4536	4.7268	408.57
Residual	21	0.2495	0.0116	
Total	23	9.6965		

Table 10: Regression results of the new model for the Vessel Doser (VD).

Var-Name	Coefficient ± Std.Err.(coeff)	t-Test	α
INTERCEPT	0.7678 ± 0.0949	8.088	< 0.0001
$\dot{V}$	0.0912 ± 0.0037	24.927	< 0.0001
d	0.1536 ± 0.0109	13.992	< 0.0001

The statistical tests, F-value > 400 and significance of the independent variables, confirm the functional correlation between the input parameters and the particle mass flux. The next step is the evaluation of the applicability of the MLR model to predict the experimental data of the VD. This is done by checking the assumptions discussed in section 2.3.1.

Linear Relationship

A linear relationship between the predicted and measured values was achieved by using the logarithmic values of the mass flux. The quality of fit (R^2) amounts to 0.9749.

Normal distribution

Figure 23 shows the residual distribution. The dotted line indicates a perfect normal distribution. The residuals follow the normal distribution in an acceptable manner.

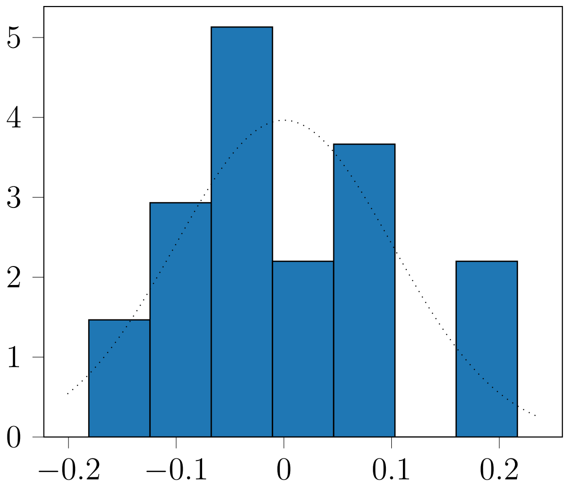

Figure 23: Histogram of the residuals for the MLR of the Vessel Doser (VD). The dotted line indicates a perfect normal distribution.

Homoscedasticity
Figure 24 shows a scatter plot of the residuals. The residuals are randomly distributed around the center line. Thus, the difference between the predicted solid mass fluxes and the experimental data underlies a random distribution. Therefore, the residuals indicate no systematic trend and are not predictable or dependent on each other. As a result the residuals are homoscedastic.

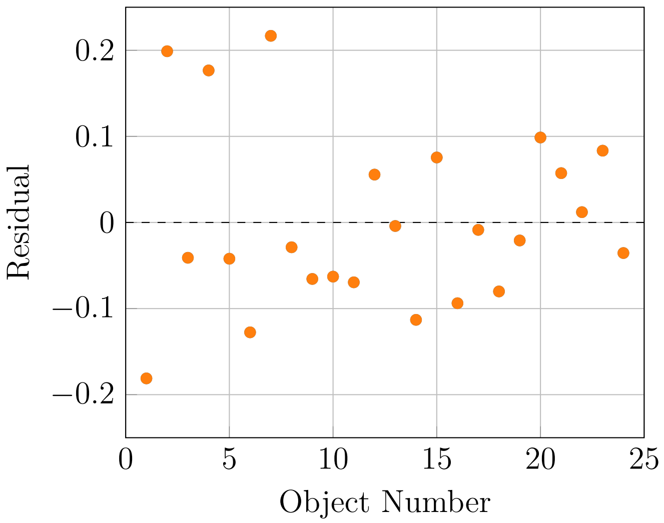

Figure 24: Scatter plot of the residuals for the Vessel Doser (VD).

Multicollinearity
The VIF does not show any correlation between the independent variables $\dot{V}$ and d, which is indicated by a VIF of 1 for each parameter:

- $VIF_{\dot{V}} = 1$
- $VIF_d = 1$

Consequently, the MLR model is suitable for the experimental data set, since it has passed the statistical tests. The functional correlation identified is given by:

$$ln(\dot{M}\ [g/s]) = 0.7678 + 0.0912 \cdot \dot{V}\ [l/min] + 0.1536 \cdot d\ [mm] \tag{26}$$

4.6 Discussion

According to the experimental data, a mass flux $\dot{M}$ between 10.07 and 56.13 g/s was observed. The statistical analysis revealed a significant influence of the total volume flow ($\dot{V}$) and outlet diameter (d) on the the solid mass flux. The share of the gas flow introduced by the FV on the total gas flow has only minor effects on the mass flux. The main effect calculation shows that $\dot{V}$ has the highest impact on the particle mass flow. The correlation between $\dot{V}$, d and $\dot{M}$ can be seen in Figure 25.

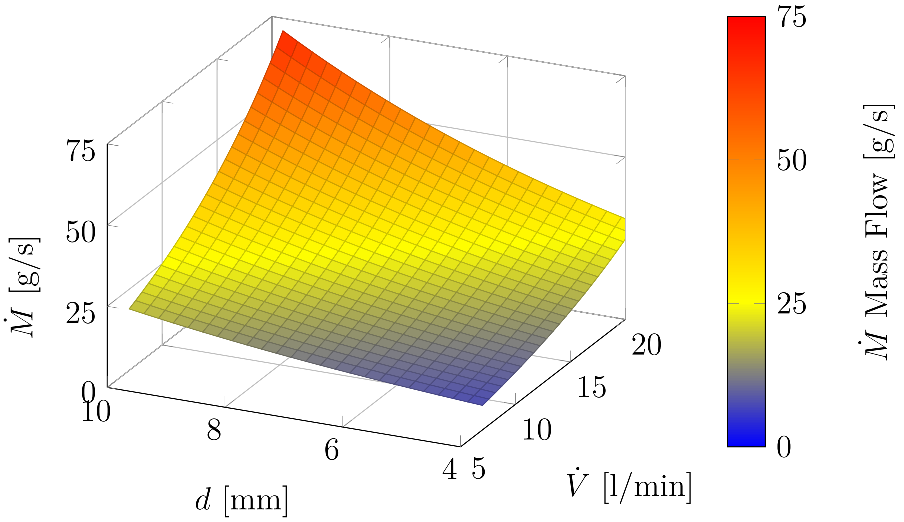

Figure 25: Surface plot of the predicted mass flux ($\dot{M}$) of the Vessel Doser (VD) as a function of the outlet diameter (d) and the total volume flow ($\dot{V}$).

The mass flow ratio can be seen in Figure 26 and shows, that it is possible to operate the dosing unit with a dense phase flow within the analysed operation condition. The gas solid flow is close to dilute phase conveying for small outlet tube diameters.

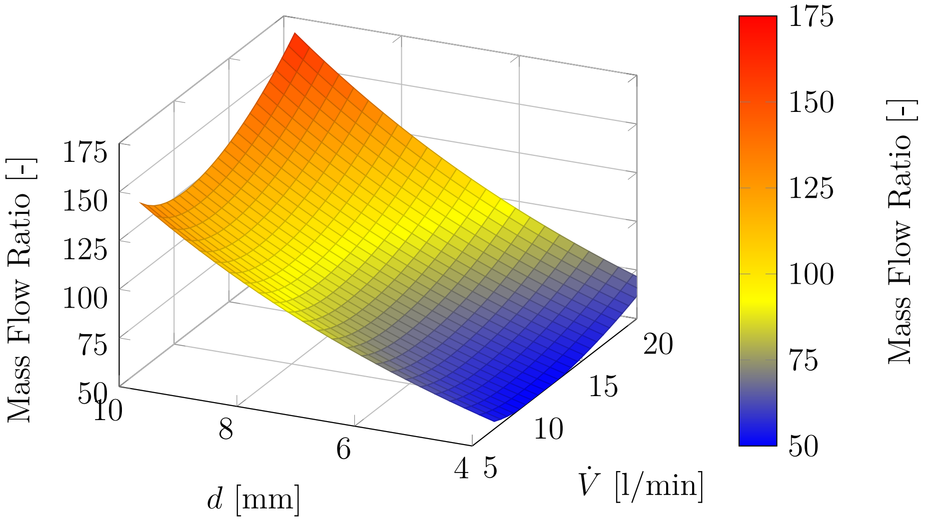

Figure 26: Surface plot of the Mass Flow Ratio ($\frac{\dot{M}_s}{\dot{M}_g}$) of the Vessel Doser (VD) as a function of the outlet tube diameter (d) and total volume flow of the carrier gas ($\dot{V}$)

Figure 27 depicts the solid-fluid flow rate ratio. By increasing the outlet tube diameter the solid-fluid flow rate ratio increases. However, there seems to be a minimum for the solid-fluid flow rate ratio at a total volume flow of about 15 l/min and a diameter of 4 mm.

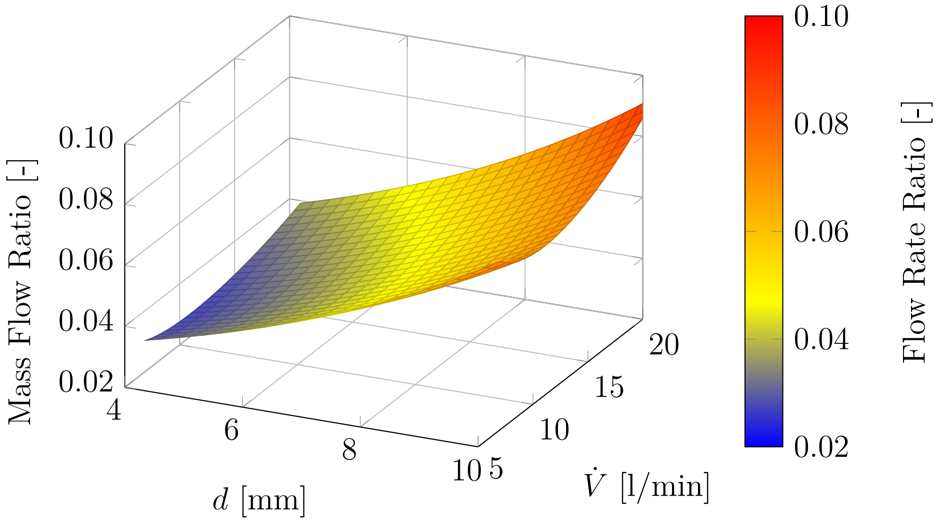

Figure 27: Surface plot of the Flow Rate Ratio ($\frac{\dot{V}_s}{\dot{V}_g}$) of the Vessel Doser (VD) as a function of the outlet tube diameter (d) and total volume flow of the carrier gas ($\dot{V}$).

The flow regimes in the VD vary between the column and the riser. Figure 28 shows the different flow regimes for the minimum and maximum $\dot{V}$ in the riser and the column of the VD for the investigated salt particles. According to Rabinovich [9] slug flow is supposed to be within the riser and plug flow within the column. However, within the column no bubbling was observed, while within the riser, slug flow and plug flow was predominant.

The Grace diagram indicates, that the the u_{mf} for the riser is only reached at the upper boundary of $\dot{V}$. The lower boundary for the riser is below the u_{mf} line. For the column, both the upper and lower boundary of $\dot{V}$ are below the fluidization point and therefore, in the state of a loosened bed. According to the calculation of u_{mf} a $\dot{V}$ of at least 60 l/min is required to reach the u_{mf} within the column. As a conclusion, the Grace diagram fits better for the column, while the Rabinovich diagram fits to the riser.

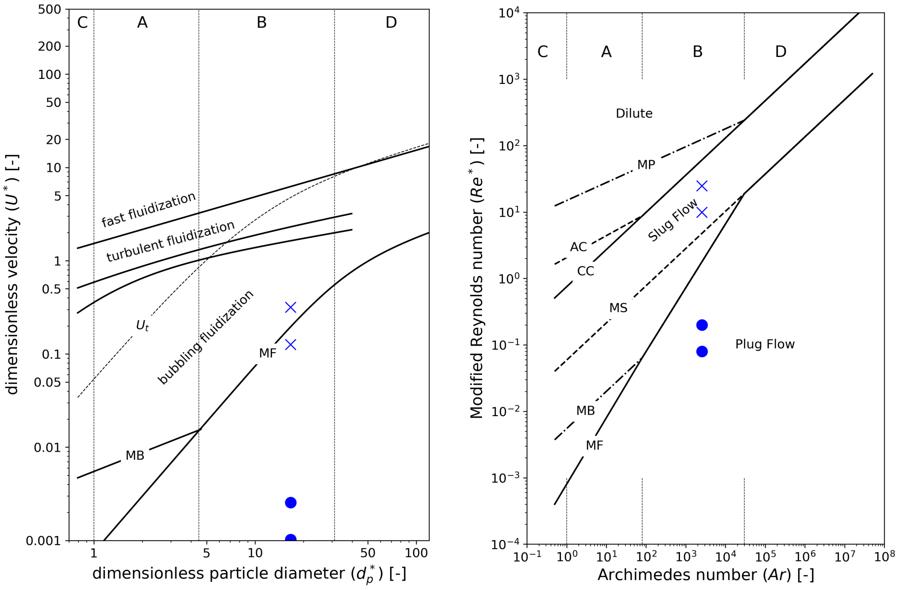

Figure 28: Characterization of flow regimes for the Vessel Doser (VD) by the Grace diagram (left) and the Rabinovich diagram (right). The dots represent the calculated flow regimes within the column and the crosses show the regimes for the riser for salt. The lower symbol represents the lower boundary of $\dot{V}$ and the upper symbol the higher boundary.

5 Revolver Doser

5.1 Dimensioning

The Revolver Doser (RD) is similar to the doser used for characterization of single coal particle combustion by Vorobiev [27] and Köser et al [30].
The dimensioning of the RD focused on achieving a mass flux of 0.5 to 1.5 g/min. Two critical design parameters were identified during the pre-evaluation: The rotating disc and the gas distribution plate.
Initial tests with small tubes, dipped into a container with pulverized coal (PC) and salt showed that about 20 to 50$\%_{vol}$ of those small tubes could be filled. One design limitation was the available stepper motor, which was limited in its rotational speed between 1 to 15 rpm.
Two discs with heights (h) of 2.13 and 3 mm and a diameter of 5 cm were designed. Each disc has 24 holes with 2 mm of diameter. The theoretical mass flux for one and 15 rotations per minute (M_{1r}) and (M_{15r}) are calculated. The calculation is realized by assessing the volume of 1 hole (V_{1o}) according to h and the diameter of 2 mm per hole. With the bulk density of 1344 kg/m³ for salt and a theoretical filling of 35$\%_{vol}$ per hole, the mass of salt within one (M_{1o}) and 24 holes (M_{24o}) were calculated. Table 11 shows the estimation of the mass flux, with 35$\%_{vol}$ filled hole. A theoretical mass flux of 0.08 g/min to 1.60 g/min is possible with the proposed disc design. Figure 29 shows the designed disc for the RD. The hole in the middle is used to install the disc on a drive shaft.

Table 11: Estimated solid mass flux of the designed Revolver Doser (RD), where (h) is the disc height, (V_{1o}) is the volume of one hole, (M_{1o}) and (M_{24o}) is the mass of salt in one and 24 holes with a theoretical filled hole of 35$\%_{vol}$ and (M_{1r}) and (M_{15r}) is the possible mass flux of salt at disc rotational speed of 1 and 15 rpm.

h [mm]	V_{1o} [m³]	M_{1o} (35 % filled) [kg]	M_{24o} (35 % filled) [kg]	M_{1r} [g/min]	M_{15r} [g/min]
2.13	$6.69 \cdot 10^{9}$	$3.15 \cdot 10^{-6}$	$7.55 \cdot 10^{-5}$	0.08	1.13
3	$9.42 \cdot 10^{-9}$	$4.43 \cdot 10^{6}$	$1.06 \cdot 10^{-4}$	0.11	1.60

Figure 29: Picture of the perforated disc used in the Revolver Doser (RD).

For the calculation of the porous plate the pressure loss (Δp) over the bed for PC was calculated. Δp was calculated assuming a porosity (ϵ) of 0.46, a solid density (ρ_s) of 1200 kg/m^3 for PC, a fluid density ρ_f of 1.2 kg/m^3 for nitrogen, gravitational force (g) of 9.81 m/s^2 and a bed height (H) of 5 cm. The estimated Δp is 317 Pa for the bed. For an optimal fluidization of a fluidized bed of reactors the pressure loss of the distribution plate should be around 0.21 times [17] of the pressure loss of the bed, which is equal to 66.57 Pa for the given RD design. A porous HDPE distribution plate of 1.6 mm with a porosity of 20-35 μm was chosen, which gives a Δp of about 1000 Pa in the operation range. This distribution plate with such a high pressure loss was chosen to prevent a possible wall-effect [18].
Gas is introduced into the RD from the "Inlet Windbox" (IWB) from the bottom through the porous distribution and the Inlet Doser (ID) at the top. The IWB combined with the distribution plate should ensure a fluidization within the particle chamber to allow a smooth rotation of the perforated disc. Carrier gas introduced through the ID conveys particles from the perforated disc towards the outlet. Through adjusting the volume flux of the carrier gas, the gas-solid ratio can be varied.

5.2 Setup

Figure 30 depicts a schematic illustration and a picture of the RD. Particles are stored in the chamber (6) and fluidized from the bottom through a porous distribution plate (5), to ensure a smooth rotation of the perforated disc (4). The gas stream for fluidization is introduced via a windbox below the porous distribution plate, through the IWB. The perforated distribution plate was a rectangle with dimensions of 40 mm x 50 mm and had a surface area of 2000 mm^2. The particles are picked up by the holes in the perforated disc and transported to a pipe at the top of the RD. A continuous gas stream from the ID is maintained in this pipe. The combination of the gas stream from the ID and the IWB ensures that the particles are blown out through the outlet and conveyed further into the collection box.

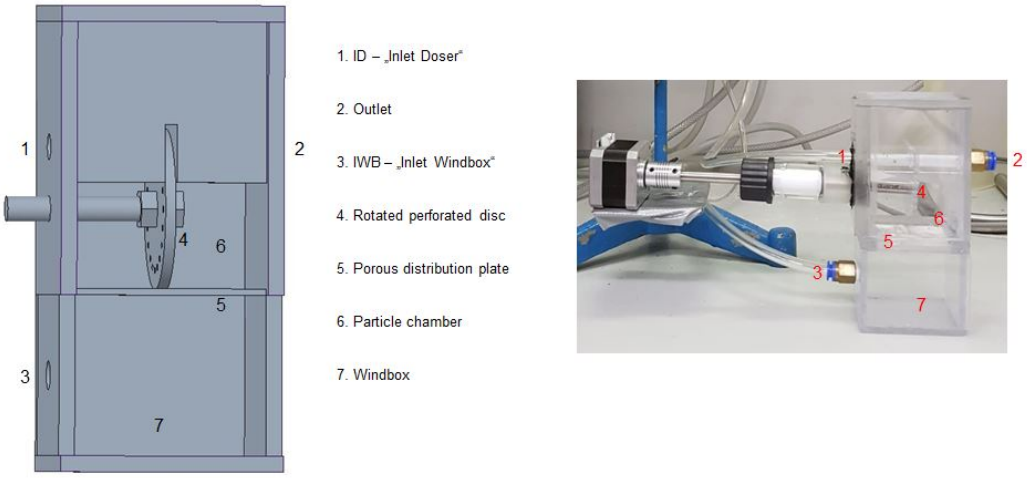

Figure 30: Schematic illustration (left) and a picture of the Revolver Doser (RD) (right).

5.3 Trial Conditions

To characterize the RD two main parameters were investigated:

- Rotational speed of the disc (RPM)
- height of the disc (h)

The gas velocities introduced through the ID and the IWB remained constant throughout all experiments. The following physical properties were used for the solid and fluid phase For the calculation of the u_{mf} and u_t for the RD:

- Solid phase - Salt (see A)
    - $d_{sv} = 400\ \mu m$
    - $\rho_s = 2160\ kg/m^3$
- Fluid phase - Air
    - $\nu_f = 1.8 \cdot 10^{-6}$ Pa $\cdot$ s
    - $\rho_f = 1.2\ kg/m^3$

The u_{mf} is 0.109 m/s and the u_t is 1.154 m/s for the salt particles. Within the particle chamber u_{mf} would be reached at 13.08 l/min, whereas u_t can be reached with a fluid volume flow of 138.48 l/min. The IWB is set to 15 l/min, which is slightly higher than the u_{mf} for the salt particles. The ID is set to 5 l/min.
Three instead of two settings are chosen for the rotational speed, since it was not clear, whether the correlation of the RPM of the disc and the particle mass flux is linear. The initial assumption was that more particles might fall out of the holes of the disc at higher rotational speeds, due to higher centrifugal forces, leading to an optimal rotational speed in the center range. This would be overlooked with two settings. Rotational speeds of 1.72, 5.99 and 13.39 1/min are used in the experiments.
To asses the influence of d_{sv}, two different particle sizes were chosen: table salt with $d_{sv} = 400\ \mu m$ and grounded table salt with $d_{sv} = 150\ \mu m$ (see B). Unfortunately, electrostatic forces caused by the friction of the particles with each other, the walls, the distribution plate and the rotating perforated plate emerged during the fluidization of salt particles with $d_{sv} = 150\ \mu m$. All attempts to ground the components of the dosing unit with cooper band failed. Therefore, it was not possible to obtain reasonable data for salt particles with $d_{sv} = 150\ \mu m$. Table 12 summarizes the 2^2 DOE matrix including a center point for the factor RPM but neglecting the influence of d_{sv}.

Table 12: DOE matrix for the Revolver Doser (RD) with two factors and a center point. RPM denotes rotational speed and h the height of the disc.

RPM $[\frac{1}{min}]$	h [mm]
1.72	2.13
5.99	2.13
13.39	2.13
1.72	3
5.99	3
13.39	3

Evaluation of the resulting particle mass flux was done by linear regression similar to the VD experiments (see section 4.3). The particles which are forced through the outlet are collected in a box, situated on a scale. Each trial lasted for 15 minutes in order to compensate the lack of sensitivity of the balance. Figure 31 shows two example trials of the RD.

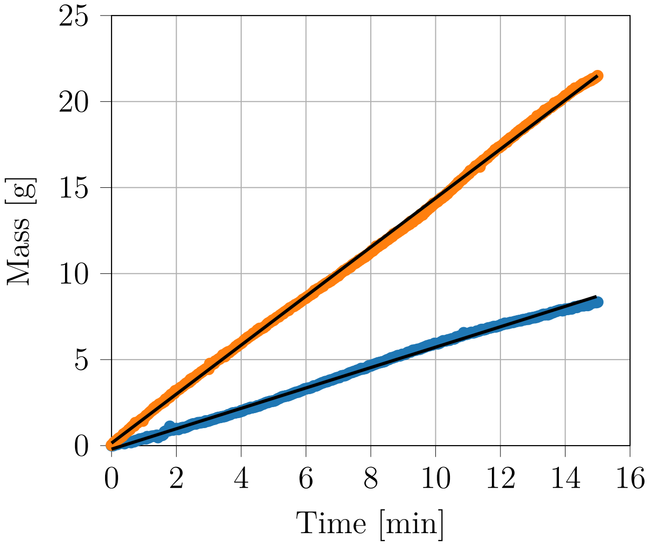

Figure 31: Two representative experimental results for the Revolver Doser (RD) including the linear regression of each trial. Blue doted: Inlet Windbox (IWB) = 15 l/min, Inlet Doser (ID) = 5 l/min, rotational speed of the disc (RPM) = 1.72 1/min, particle size (d_{sv}) = 400 µm; orange doted: ID = 5 l/min, IWB = 15 l/min, RPM = 13.39 1/min, d_{sv} = 400 µm.

5.4 Revolver Doser (RD) DOE Results

Table 13 summarizes the results for the experimental trials of the RD. Three trials were made for each experimental setting. The mean mass flux are used for the subsequent evaluations.

Table 13: The results of the Revolver Doser (RD) trials including the different disc heights (h) and rotational speeds (RPM).

Disc height h [mm]	Rotational speed RPM [1/min]	Average [g/min]	Trial 1 [g/min]	Trial 2 [g/min]	Trial 3 [g/min]
3	13.39	1.35	1.34	1.3	1.42
3	5.99	0.74	0.72	0.73	0.77
3	1.72	0.43	0.43	0.42	0.44
2.13	13.39	0.80	0.80	0.82	0.77
2.13	5.99	0.44	0.44	0.42	0.45
2.13	1.72	0.28	0.27	0.29	0.28

Linear regressions were made for the two discs to confirm a linear relationship between the RPM and and the particle mass flux. For these regressions the center points were included. Figure 32 shows the result for these regression. The orange dots indicate the disc with 2.13 mm height and blue the disc with 3 mm height. The R^2 of both regressions were above 0.99. Thus, a linear relationship between the RPM and the particle mass flux is justified.

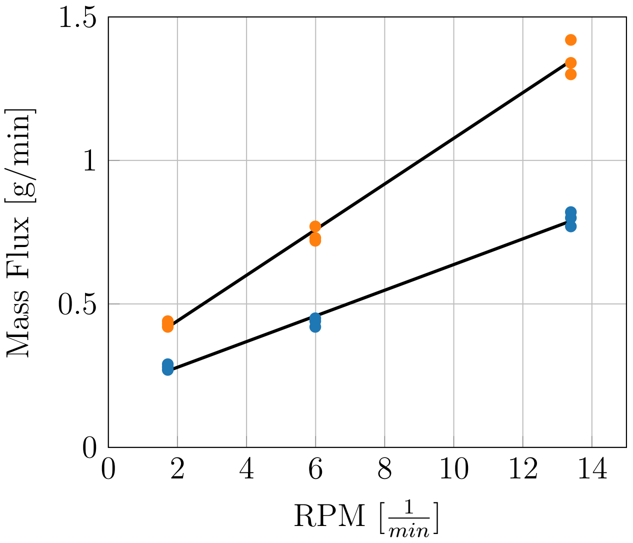

Figure 32: Regressions of the rotational speed of the disc (RPM) and the mass flux for the two different disc heights (h). Orange: h = 3 mm; Blue: h = 2.13 mm.

Table 14 shows the DOE matrix including the transformed settings ("-1" and "+1") of the factors and the interaction of h x RPM. The average mass fluxes were calculated out of he three trials per experimental point.

Table 14: DOE matrix for the Revolver Doser (RD). The mass fluxes are shown with their corresponding settings including their interaction.

h	RPM	h x RPM	Avg. Mass Flux [g/min]
+1	+1	+1	1.34
+1	-1	-1	0.72
-1	+1	-1	0.43
-1	-1	+1	0.8

Figure 33 shows the effects for h (left), RPM (middle) and the interaction of h x RPM (right). By increasing h and RPM, the mass flux rises. Furthermore, h and RPM are interacting with each other.

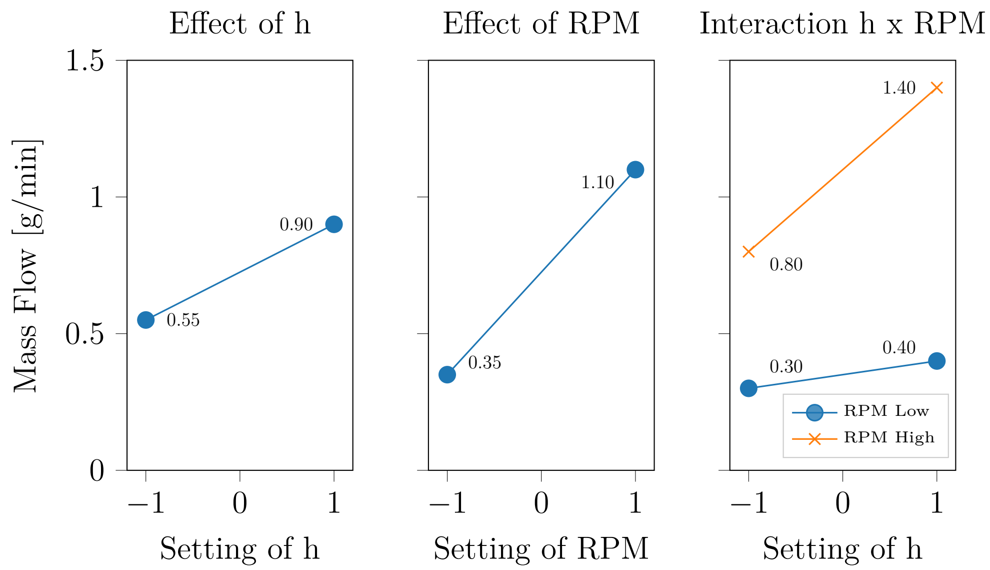

Figure 33: Effect and interaction plots of the Revolver Doser (RD) DOE.

Figure 34 shows the calculated main effect for the two factors of the RD and their interaction. The factor RPM has a twice as high influence on the mass flux compared to the factor h.

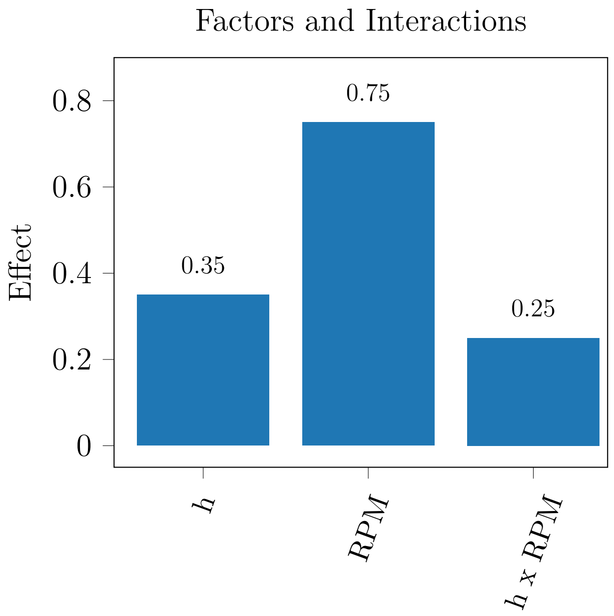

Figure 34: Main effects of all factors and their interactions for the Revolver Doser (RD).

5.5 Statistics

5.5.1 First Approach

A MLR and an ANOVA was performed for statistical analysis. Figure 35 shows the regression of the predicted mass flux of the RD versus the experimental data. The predicted mass fluxes seem to be higher in the range between 0.5 and 1 g/min and lower in the range below 0.5 g/min and above 1.5 g/min compared to the experimental data.

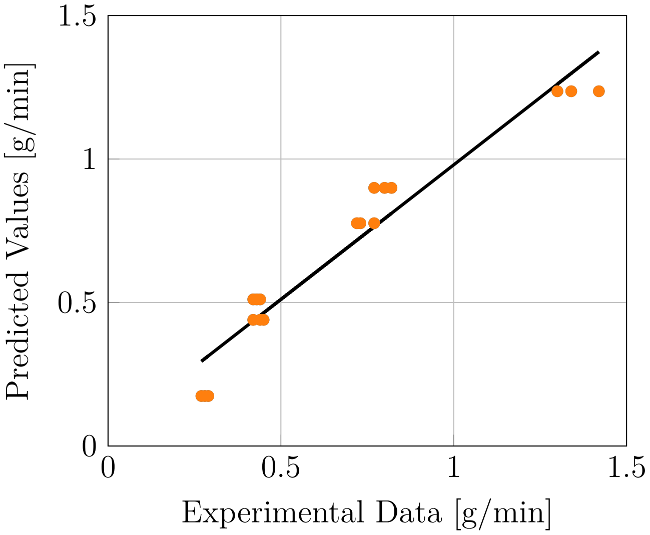

Figure 35: Linear relationship of the predicted values versus the experimental data of the Revolver Doser (RD).

The quality of the linear regression between the experimental data and the predicted mass fluxes indicate a bad fit and can be summarized by:

- SDR: 0.3628
- R^2: 0.9358

5.5.2 Final Approach

Similar to the VD the model is adapted by taking the logarithmic values of the mass flux. Figure 36 visualizes the final model. The predicted values and the experimental data show a linear relationship with an R^2 of 0.9751. Hence, an improvement of the previous model has been achieved.

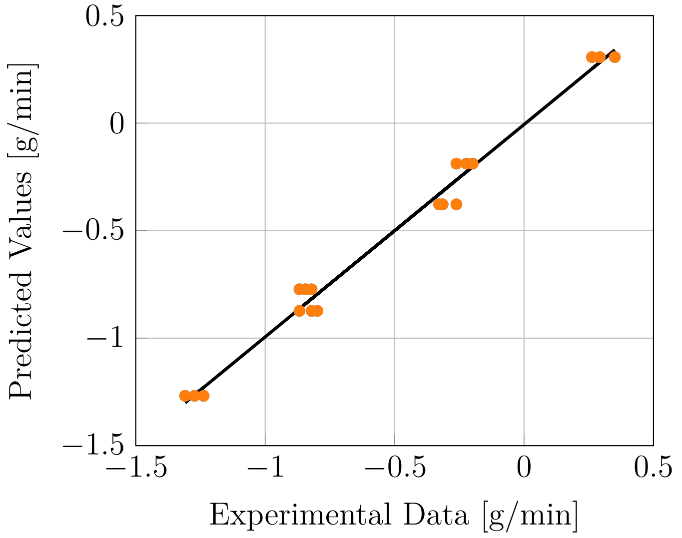

Figure 36: Linear relationship of the predicted values versus the experimental data of the final model for the Revolver Doser (RD).

The quality of fit of the final model for the RD can be summarized by:

- SDR: 0.0889
- R^2: 0.9751

Table 15 shows the results of the ANOVA. The calculated F-ratio of 293.48 indicates, that the model is not generated by random effects. Table 16 shows the regression results of the model. Both independent variables h and RPM show a small α value, which means that they are significant.

Table 15: F-statistic of the improved model for the Revolver Doser (RD). DF, SS, MS denote the degree of freedom, sums of squares and means of squares.

	DF	SS	MS	F-Ratio
Regression	2	4.6366	2.3183	293.48
Residual	15	0.1185	0.0079	
Total	17	4.7551		

Table 16: Regression results of the final approach for the Revolver Doser (RD) including the coefficients, the result of the t-Test and the α values.

Variable	Coefficient ± Std.Err.(coeff)	t-Test	α
INTERCEPT	-2.5821 ± 0.1289	-20.02	<0.0001
h [mm]	0.5491 ± 0.0482	11.40	<0.0001
RPM [1/min]	0.0929 ± 0.0043	21.38	<0.0001

A correlation between the two significant independent variables and the mass flux is confirmed according to the results of the MLR and the ANOVA. The applicability of the MLR model is subsequently evaluated as discussed in Section 2.3.1.

Linear Relationship

The model for the RD could be improved by using the logarithmic values of the mass flux. The R^2 changed from 0.9358 to 0.9751 for the regression of the predicted mass flux and the experimental data. Therefore, a good quality of fit was achieved and a linear relationship is confirmed.

Normal distribution

Figure 37 shows the distribution of the residuals for the RD. The dotted line indicates a perfect normal distribution. The residuals fit the normal distribution well.

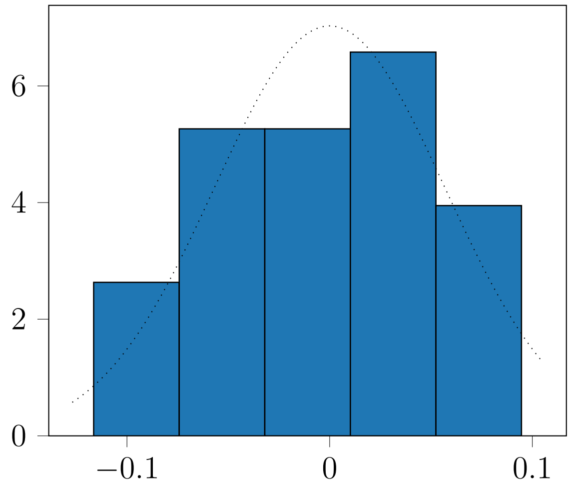

Figure 37: Histrogram of the residuals for the Multiple Linear Regression (MLR) of the Revolver Doser (RD). The dotted line indicates a perfect normal distribution.

Homoscedasticity

Figure 38 shows a scatter plot of the residuals for the RD model. The distribution of the residuals are random around the center line. Therefore, the difference of the predicted values and the experimental data are randomly disturbed, which means that the residuals are homoscedastic.

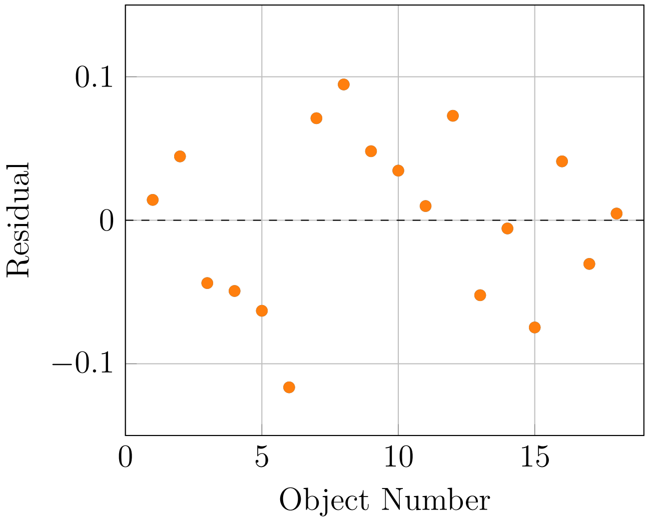

Figure 38: Scatter plot of the residuals for the Revolver Doser (RD).

Multicollinearity

The VIF does not show any correlation between the independent variables h and RPM, which is indicated by a VIF of 1.

- $VIF_h = 1$
- $VIF_{RPM} = 1$

The MLR for the RD with salt particles of $d_{sv} = 400\ \mu m$ passed the statistical tests and is therefore suitable to model the obtained data set. Equation (27) shows the identified functional correlation of the data set.

$$ln(\dot{M}\ [g/min]) = -2.5821 + 0.5491 \cdot h\ [mm] + 0.0929 \cdot RPM\ [1/min] \quad (27)$$

5.6 Vertical Setup

The RD was turned 90 degrees into an upright position in an attempt to overcome electrostatic influences due to fluidization of particles, which emerged while fluidizing particles with $d_{sv} = 150\ \mu m$ and to compare different particle sizes. The outlet of the dosing unit was now situated at the bottom and the perforated disc was in a vertical position. Figure 39 depicts the vertical set up of the RD.

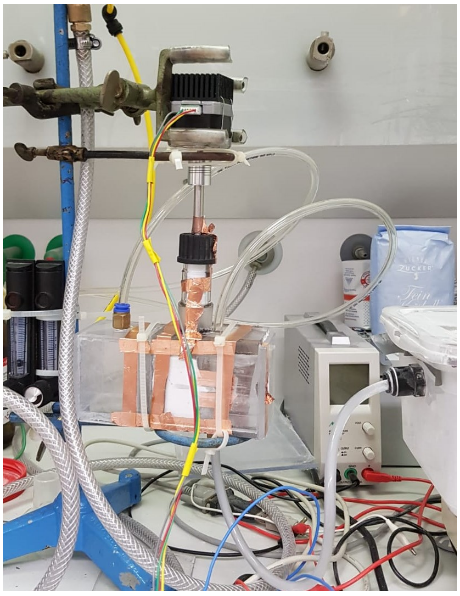

Figure 39: The Revolver Doser (RD) rotated 90 degrees into an upright position.

The trials were performed without any gas stream from the IWB, but a constant ID flow rate of 5 l/min of carrier gas. The rotational speeds (RPM) were set to 13.39, 5.99 and 1.72 1/min for a total trial length of 5 minutes, similar to the trial conditions for the RD discussed in Section 5.3.
The estimation of possible mass flux is similar to the calculation in section 5.1 for the RD. Table 17 shows the theoretical mass flux, according to the dimensions of the perforated plates, with a bulk density of salt of 1344 kg/m^3. Unlike the RD, the vertical setup is estimated with a theoretically filled hole of 100%. The values indicate an interesting option for the desired $\dot{M}$ range of 0.5 to 1.5 g/min.

Table 17: Estimated solid mass flux of the vertical Revolver Doser (RD) setup, where (h) is the disc height, (V_{1o}) is the volume of one hole of a disc, (M_{1o}) and (M_{24o}) is the mass of salt in one and 24 holes with a theoretical filled hole of 35 % and (M_{1r}) and (M_{15r}) is the possible mass output of salt at disc rotational speed of 1 and 15 1/min.

h [mm]	V_{1o} [m^3]	M_{1o} [kg]	M_{24o} [kg]	M_{1r} [g/min]	M_{15r} [g/min]
2.13	$6.69 \cdot 10^{-9}$	$8.99 \cdot 10^{-6}$	$2.16 \cdot 10^{-4}$	0.22	3.24
3	$9.42 \cdot 10^{-9}$	$1.27 \cdot 10^{-5}$	$3.04 \cdot 10^{-4}$	0.30	4.56

Unlike the horizontal RD, the vertical RD showed performance problems with salt particles with $d_{sv} = 400\ \mu m$. Particles with larger sizes wedged between the rotated perforated disc and the vessel wall. The rotation stopped and the stepper motor heated up rapidly. Thus, leading to the stop of the experimental trials with particles with $d_{sv} = 400\ \mu m$.
Only two trials were made per experimental point, since the setup was not designed to perform in this configuration and the expectation to compare two different particle sizes were not met. Table 18 shows the results for the trials of the vertical RD.

Table 18: Results of the vertical Revolver Doser (RD) setup tests including the disc heights (h), rotational speed of the disc (RPM) and mass fluxes ($\dot{M}$).

h [mm]	RPM $\left[\frac{1}{min}\right]$	$\dot{M}$ AVG [g/min]	$\dot{M}$ Trial 1 [g/min]	$\dot{M}$ Trial 2 [g/min]
2.13	13.39	6.23	4.99	7.47
2.13	5.99	2.755	2.52	2.99
2.13	1.72	0.685	0.72	0.65
3	13.39	6.93	6.67	7.19
3	5.99	2.8	2.15	3.45
3	1.72	0.97	0.97	0.97

The results show a high variation between trial 1 and 2 of the $\dot{M}$ for the experimental points h = 2.13 mm, RPM = 13.39 1/min and h = 3 mm, RPM = 5.98 1/min. This might be due to handling issues and the problem that the RD was not designed for this setup. Figure 40 shows the results for the vertical RD with salt particles with $d_{sv} = 150$ μm. Furthermore, $\dot{M}$ is higher than the theoretical calculation (see Table 17), which indicates that many particles are entering the outlet tube without being transported by the rotating perforated disc.

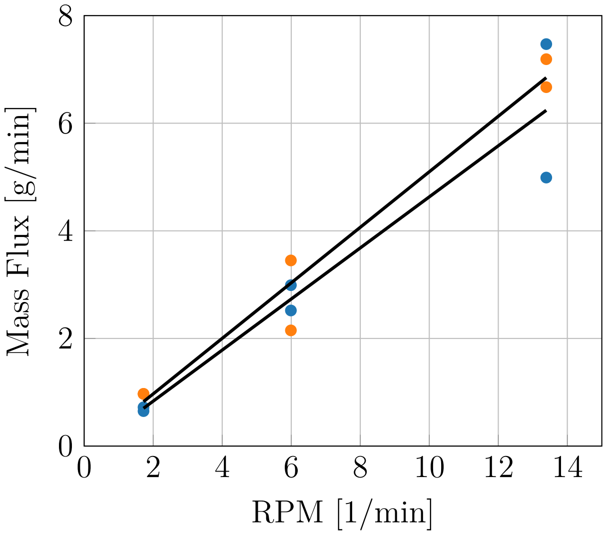

Figure 40: Regression result of the rotational speeds (RPM) and $\dot{M}$ for two different disc heights (h) of the vertical Revolver Doser (RD) setup with salt particles of $d_{sv} = 150$ μm. Blue: h = 2.13; Orange: h = 3.

The test revealed that the setup is not optimized for the vertical operation and has to be re-designed for vertical operation. Particles can enter the outlet tube without being transported by the holes of the perforated disc, since the slit between the rotating disc and the outlet tube is not sealed. Furthermore, Figure 40 shows that the results of the trials for h = 2.13 and h = 3 do not differ significantly and more repetitions would be necessary to obtain statistical significant results.

5.7 Coal Tests

Trials were carried out with PC as solid and nitrogen as fluid phase after successfully evaluating the MLR for the RD with salt particles. Following physical properties were used for the fluid and solid phase for the calculation of u_{mf} and u_t:

- Solid phase - pulverized coal (PC)
  - $d_{sv} = 75\ \mu m$
  - $\rho_s = 1200\ kg/m^3$
- Fluid phase - nitrogen
  - $\nu_f = 1.7 \cdot 10^{-6} Pa \cdot s$
  - $\rho_f = 1.14\ kg/m^3$

The u_{mf} of the coal particle is 0.002 m/s and the u_t is 0.133 m/s. A fluid flow of at least 0.24 l/min is necessary to reach the u_{mf} within the particle chamber of the RD . For u_t a fluid flow of 15.6 l/min is needed.

Coal particles fluidized with nitrogen are situated in Geldart group A, which indicates a good fluidization potential. However, initial tests showed a strong wall-effect [18] during the fluidization. Figure 41 shows the inside of the RD after a trial with coal particles and nitrogen, which indicates that the particles were not fluidized properly and the carrier gas passed through the chamber near the rotating perforated disc. For the experimental trials the IWB is set to 1 l/min, which was sufficient to reach the u_{mf} within the windbox, while the ID flow is maintained at 5 l/min. Two different disc heights (2.13 and 3 mm) are used, which is similar to the previously discussed salt tests.

Three RPM settings are chosen (1.72, 5.99 and 13.39), to confirm a linear relationship between the mass flux and RPM.

In contrary to the salt tests, the trials for the coal tests were only executed for 30 seconds, since the conveying of particle stopped rapidly, due to a lack of fluidization.

The evaluation of the resulting mass fluxes was similar to the previously discussed salt tests. A linear regression was performed between mass and time. Figure 31 shows examples for the linear regressions of the mass over time of salt particles.

Table 19 summarizes the obtained data of the successful coal tests with the RD. The R^2 is also given to indicate the linearity of the regression for the mass fluxes.

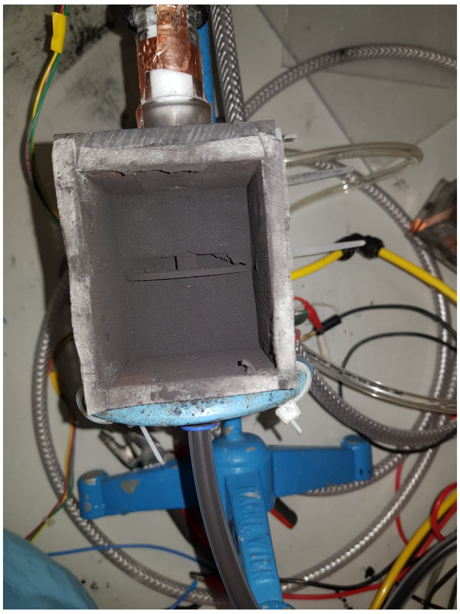

Figure 41: Picture of the particle chamber of the Revolver Doser (RD) filled with coal

Table 19: Results of the coal tests including the disc height (h), rotational speed of the disc (RPM), mass flux and the corresponding R^2 of the linear regression for the mass flux.

$\dot{M}$ [g/min]	R^2 [-]	h [mm]	RPM $\frac{1}{min}$
1.06	0.95	2,13	13.39
1.24	0.97	2.13	13.39
0.77	0.96	2.13	5.99
0.73	0.95	2.13	5.99
0.94	0.86	2.13	5.99
0.45	0.93	2.13	1.72
0.28	0.64	2.13	1.72
1.12	0.99	3.00	13.39
0.05	0.13	3.00	13.39
1.67	1.00	3.00	13.39
1.18	0.83	3.00	5.99
0.67	0.98	3.00	5.99
0.49	0.96	3.00	1.72

The significant variation of the R^2 indicates problems with the experimental trials. Figure 42 shows the data of two trials with low R^2 including their linear regression. Both trials show an extreme fluctuation of the recorded data. Furthermore, results of some experiments with similar settings vary visibly. For instance, the experiments h = 2.13 mm and RPM = 13.39 1/min, results in 1.06 and 1.24 g/min, which is a variation of around 15 %. Due to the lack of data and the inability to replicate experimental results, no detailed statistical analysis was performed for the coal tests.

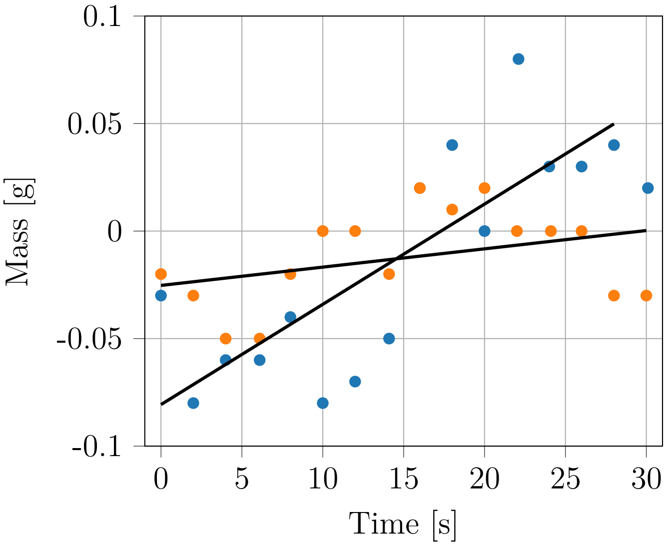

Figure 42: Two trials with a high R^2 obtained for the coal tests in the Revolver Doser (RD). Orange dots: M = 0.05, R^2 = 0.13, RPM = 13.39 1/min, h = 3 mm. Blue dots: M = 0.28 g/min, R^2 = 0.64 RPM = 1.72 1/min, h = 2.13 mm.

Figure 43 shows the regression of the $\dot{M}$ and the RPM of the coal tests neglecting any data with an R^2 below 0.9. The remaining data is insufficient for a significant statistical statement.

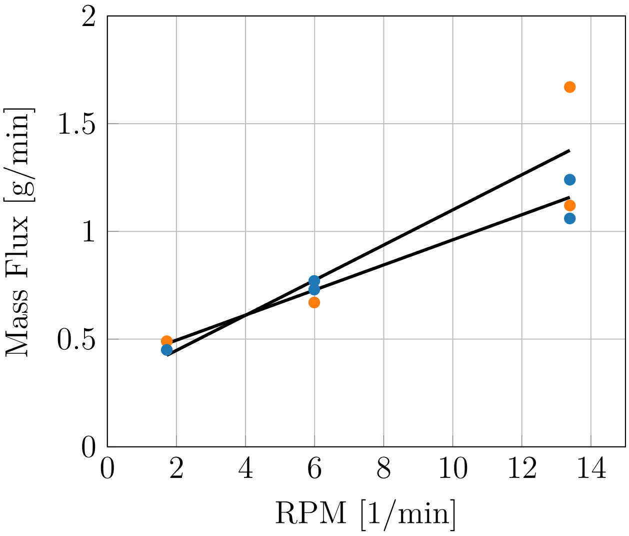

Figure 43: Regression of the rotational speed of the discs (RPM) and the mass flux ($\dot{M}$) for the two different disc heights (h) of the coal tests, while neglecting any data with and R^2 lower 0.9. Blue: h = 2.13 mm; Orange: h = 3 mm;

5.8 Discussion

The statistical analysis for the RD revealed a significant influence of the RPM and the disc height for conveying salt particles of $d_{sv} = 400\ \mu m$. Furthermore, the tested range showed that RPM and $\dot{M}$ are linearly correlated. $\dot{M}$ can be adjusted with the analysed factors and settings between 0.28 and 1.35 g/min. The results of the DOE show that the influence of RPM on $\dot{M}$ is twice as high as h. Increasing both parameter h and RPM gives higher $\dot{M}$. Figure 44 shows the resulting correlation of h, RPM and $\dot{M}$ according to Equation 27.

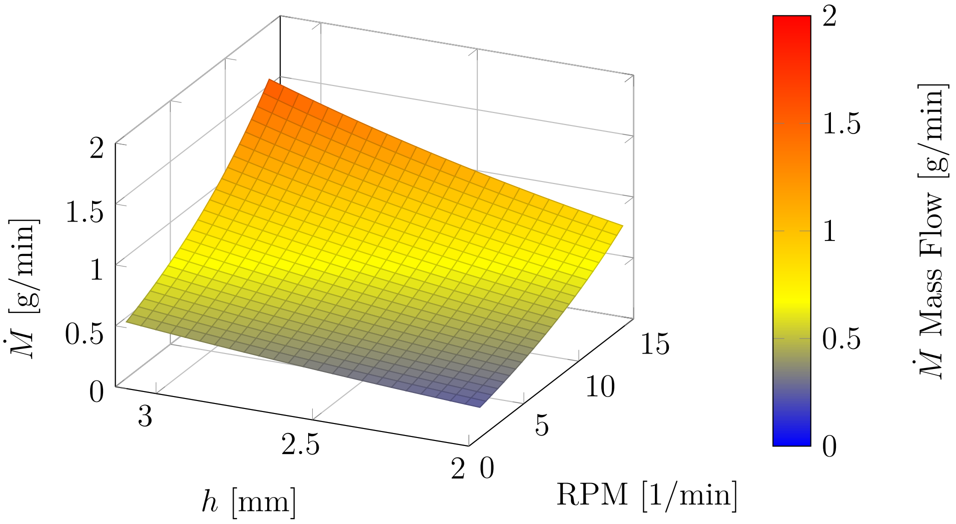

Figure 44: Surface plot of the predicted mass flux $\dot{M}$ of the Revolver Doser (RD) with varying disc height (h) and rotational speed of the disc (RPM).

Figure 45 depicts the surface plot of the mass flow ratio with varying h and RPM. The transition from dense-phase conveying to dilute-phase happens at a solid to gas ratio of around 30. Thus, the RD cannot be operated in the dense-phase regime under the investigated conditions.

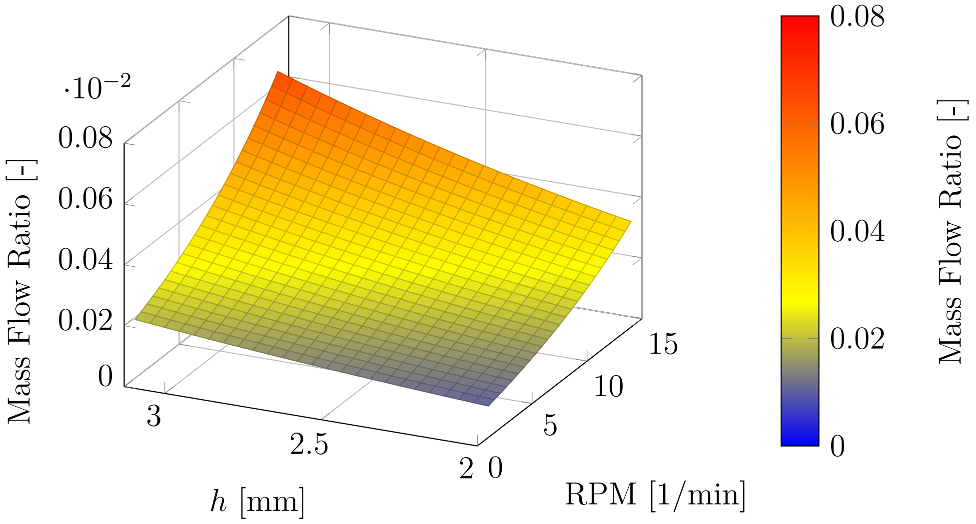

Figure 45: Surface plot of the Mass Flow Ratio ($\frac{\dot{M}_s}{\dot{M}_g}$) of the Revolver Doser (RD) with varying disc height (h) and rotational speed of the disc (RPM).

Figure 46 shows the flow rate ratio of the RD. In general, the flow rate ratio is in the dilute-phase regime. The flow rate ratio however increases with higher h and RPM, like the mass flow ratio in Figure 45 and the $\dot{M}$ in Figure 44, because the total volume flow of the carrier gas was kept constant.

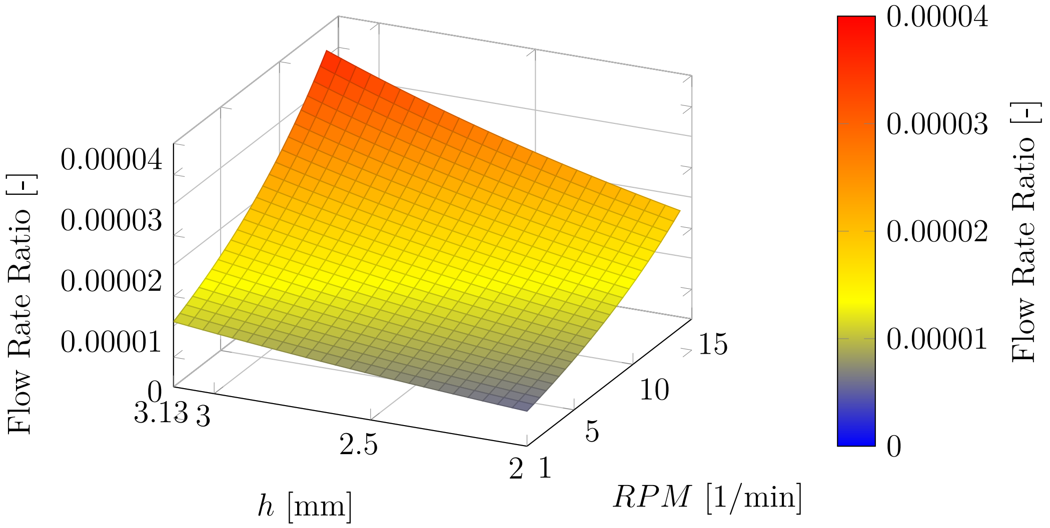

Figure 46: Surface plot of the Flow Rate Ratio ($\frac{\dot{V}_s}{\dot{V}_g}$) of the Revolver Doser (RD) with varying disc height (h) and rotational speed of the disc (RPM)

The flow regimes of the RD within the particle chamber and the outlet were assessed. Figure 47 shows the flow regimes for the coal and salt particles according to the Rabinovich and Grace diagram. The Rabinovich diagram indicates plug flow within the particle chamber for both salt and coal particles. For the outlet however, the Rabinovich diagram indicates slug flow for coal and plug flow for salt particles. According to Grace, bubbling fluidization is supposed to occur within the particle chamber and fast fluidization above u_t within the outlet, which coincides with the observation during the experiments. Plug flow did not occur during the experiments within the particle chamber. However, fluidization of the salt particles was observed. Therefore, the Grace diagram presents a good representation of the flow regime for the outlet and the particle chamber within the RD.

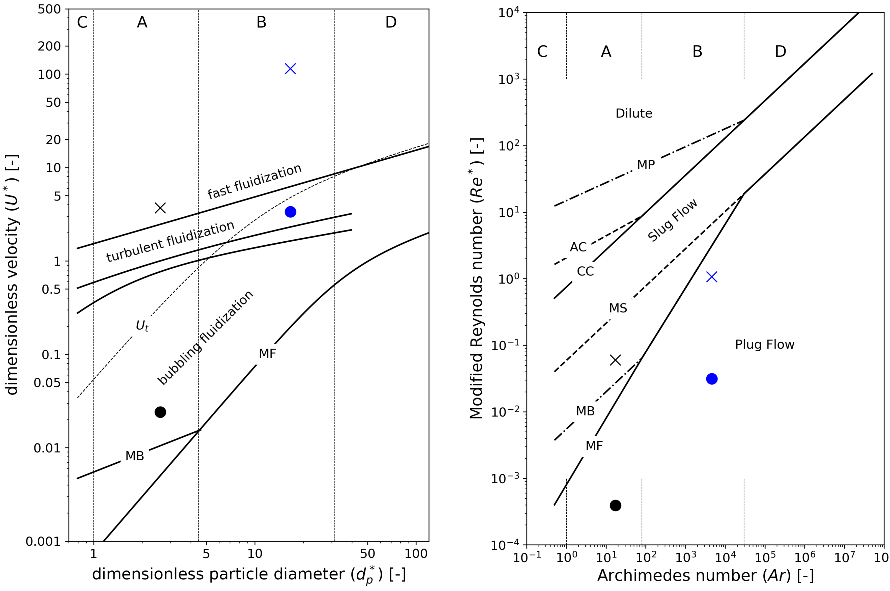

Figure 47: Characterization of flow regimes for the Revolver Doser (RD), by the Grace diagram (left) and the Rabinovich diagram (right). The dots represent the calculated flow regimes within the particle chamber, while the crosses represent the flow regime within the outlet for salt (blue) and pulverized coal (black).

Due to electrostatic forces it was not possible to perform experiments with grounded salt particles of $d_{sv} = 150\ \mu m$. Further adjustments of the RD would be necessary to enable these investigations.

In an attempt to surpass the electrostatic issues, the RD was turned 90 degrees into an upright position. The range of the achieved $\dot{M}$ for particles

$d_{sv} = 150\ \mu m$, is between 0.72 and 6.93 g/min, which is in the required range. Unfortunately, the replication of different experimental points was not possible and, therefore, no statistical analysis was possible. Furthermore, conveying particles with $d_{sv} = 400\ \mu m$ in the vertical setup was not possible, because larger particles wedged between the disc and the vessel wall, leading to the overheating of the stepper motor.

Finally, coal tests were performed with particles $d_{sv} = 75\ \mu m$ and nitrogen carrier gas. Although no statistical analysis was performed, the measured $\dot{M}$ of various experiments span a range of 0.05 to 1.24 g/min, which is the required range.

6 Conclusion

This thesis examined dosing units for a novel test reactor to investigate the conversion characteristics of pulverized coal (PC). A literature review revealed four main dosing concepts which are used for lab scale operation: Vessel, Revolver, Venturi and Mechanical Screw Doser. The Vessel and the Revolver Doser appeared to be promising concepts for the operation as dosing units for the novel reactor and were further investigated.

The Vessel Doser (VD) and Revolver Doser (RD) were successfully designed, constructed and characterized with salt particles and air. Due to the good results of the RD, further tests with PC and nitrogen were performed. These tests revealed operation problems. Finally, the RD was also operated in a vertical setup.

Vessel Doser

Experimental data showed that the VD is sensitive to the diameter of the outlet tube (d) and the total gas volume flow ($\dot{V}$). The positioning of the gas feeding valves into the column of the VD showed to have no impact on the resulting mass flux ($\dot{M}$).

A MLR was successfully developed to predict the $\dot{M}$ with two independent variables: d and $\dot{V}$. Furthermore, the flow regimes in the column and the riser of the VD were analyzed with Grace [19] and Rabinovich diagrams [9]. The flow regime in the column of the VD show a good agreement with the Grace diagram [19], while the riser complies with the Rabinovich diagram [9].

Although it is possible to operate the VD in dense phase, it is not possible to reach $\dot{M}$ of about 0.5 to 1.5 g/min with this setup.

Revolver Doser

Analysis of the RD with salt particles with $d_{sv} = 400\ \mu m$ showed an influence of the RPM and h on $\dot{M}$. However, the influence of RPM is twice as high as the influence of h. Mass fluxes between 0.28 and 1.42 g/min were observed throughout the experiments. According to the desired range of 0.5 to 1.5 g/min, the RD would be a perfect fit as a dosing unit for the novel test reactor. Further analysis of the RD tests enabled the development of a MLR, which predicts the $\dot{M}$ based on h and RPM. Unfortunately, the materials used to build the RD caused electrostatic problems. Multiple attempts to ground the inner chamber with meshes and copper strips failed. Salt particles with d_{sv} = 150 mm caused significant problems. Design and material changes, however, may improve this situation. The design itself can be improved by minimizing the contact areas of the rotating perforated plate and the particle chamber walls.

Vertical Revolver Doser Setup

Turning the RD by 90 degrees resulted in $\dot{M}$ of up to 6.93 g/min. According to theoretical calculations a $\dot{M}$ of only 4.56 g/min at a rotation speed of 15 rpm was expected. Hence, particles were able to enter the outlet tube through a gap between the disc and the dosing unit wall. Another design problem emerged during the tests with salt particles of $d_{sv} = 400$ mm: Particles wedged between the rotating perforated disc and the wall of the particle chamber. As a result the disc was not able to rotate and the stepper motor overheated. As a summary, the idea of the vertical RD looks promising, but needs a different design approach. Direct suggestions would be to have a setup where the perforated plate can rotate near the bottom of the dosing unit to minimize the dead storage below the plate. Furthermore, design adjustments are necessary to prevent particles from entering the outlet tube through the gap between the rotating disc and the particle chamber walls.

Revolver Doser Coal Tests

Coal tests with the RD turned out to be problematic, due to fluidization problems which are caused by the wall-effect in the particle chamber. The results of the coal test for the RD, showed a $\dot{M}$ in the range of 0.05 to 1.24 g/min, which would fit the required range. Future work should include a design approach which allows a higher particle bed hight and a porous plate with a higher pressure loss, to ensure a smooth fluidization of PC.

7 Outlook

According to the results, future work should focus on the optimization of the RD. Maintaining a constant mass flux in the desired range of 0.5 to 1.5 g/min is possible for salt particle of $d_{sv} = 400\ \mu m$. For PC with $d_{sv} = 75\ \mu m$ however, the design and the utilized materials need to be improved before the RD is applicable as a dosing unit for the novel test reactor. Therefore, future design should take into account for the following issues:

- The reduction of dead volume below the rotating perforated disc, easy accessibility to refill particles into the particle chamber
- Minimizing friction of particles, chamber wall and rotating perforated plate
- Increase bed heights of particles to prevent the wall-effect [18] from occurring
- Implement a possibility to seal the dosing unit to be able to apply pressure into the particle chamber

For the selection of the utilized materials of the RD the following should be considered:

- Increase the pressure loss through a thicker or different porous distribution plate to eliminate the Wall-Effect [18]
- Utilize conducting materials as chamber walls to be able to ground the device and therefore eliminate the electrostatic charge of particles

With the discussed improvements, the RD can be implemented as a PC dosing unit for the novel lab-scale test reactor at Technische Universität Wien.

A Sieve Analysis 500 μm

Table 20: First sieve analysis of salt - 1021.8 g

Upper Limit	Lower Limit	Gross Mass	Tare weight	Net. Mass	x_i	d_{pi}	$x_i \cdot d_{pi}$
μm	μm	[g]	[g]	[g]	[-]	[-]	[-]
1000	800	277.47	265.4	12.07	0.0118	900	10.6385
800	630	446.98	261.23	185.75	0.1819	715	130.0668
630	500	580.77	250.3	330.47	0.3236	565	182.8573
500	400	457.99	241.3	216.69	0.2122	450	95.4955
400	315	395.18	225.68	169.5	0.1660	357.5	59.3441
315	224	531.44	450.73	80.71	0.0790	269.5	21.3019
224	200	235.24	224.12	11.12	0.0109	212	2.3087
200	180	335.76	329.41	6.35	0.0062	190	1.1816
180	125	339.38	333.53	5.85	0.0057	152.5	0.8737
125	80	219.97	218.7	1.27	0.0012	102.5	0.1275
80	0	193.95	192.63	1.32	0.0013	40	0.0517
			Σ Net. Mass [g]:	1021.1		d_p:	504.25

Table 21: Second sieve analysis of salt - 1007.51 g

Upper Limit μm	Lower Limit μm	Gross Mass [g]	Tare weight [g]	Net. Mass [g]	x_i [-]	d_{pi} [-]	$x_i \cdot d_{pi}$ [-]
1000	800	276.32	265.67	10.65	0.0106	900	9.5175
800	630	431.96	262	169.96	0.1688	715	120.6659
630	500	582.54	251.41	331.13	0.3288	565	185.7713
500	400	457.97	242.08	215.89	0.2144	450	96.4666
400	315	399.88	226.23	173.65	0.1724	357.5	61.6428
315	224	532.72	451.8	80.92	0.0804	269.5	21.6544
224	200	235.5	224.2	11.3	0.0112	212	2.3787
200	180	335.73	329.95	5.78	0.0057	190	1.0905
180	125	338.84	333.62	5.22	0.0052	152.5	0.7904
125	80	219.95	218.66	1.29	0.0013	102.5	0.1313
80	0	193.89	192.59	1.3	0.0013	40	0.0516
			Σ Net. Mass [g]:	1007.09		d_p:	500.16

Table 22: Third sieve analysis of salt - 1006.89 g

Upper Limit μm	Lower Limit μm	Gross Mass [g]	Tare weight [g]	Net. Mass [g]	x_i [-]	d_{pi} [-]	$x_i \cdot d_{pi}$ [-]
1000	800	276.84	265.84	11	0.0109	900	9.8355
800	630	427.75	262.47	165.28	0.1642	715	117.4050
630	500	583.71	251.87	331.84	0.3297	565	186.2677
500	400	455.48	242.26	213.22	0.2118	450	95.3237
400	315	404.95	226.67	178.28	0.1771	357.5	63.3197
315	224	534.97	452.11	82.86	0.0823	269.5	22.1852
224	200	234.92	224.34	10.58	0.0105	212	2.2283
200	180	335.96	330.08	5.88	0.0058	190	1.1099
180	125	338.56	333.81	4.75	0.0047	152.5	0.7197
125	80	219.93	218.68	1.25	0.0012	102.5	0.1273
80	0	194.24	192.62	1.62	0.0016	40	0.0644
			Σ Net. Mass [g]:	1006.56		d_p:	498.59

The d_p of the individual tests were 504.25 µm, 500.16 µm and 498.59 µm.
$d_p = 500\,\mu m$
$d_{sv} = 400\,\mu m$ - according to Equation 1 with an assumed form factor (ϕ) of 0.8.

B Sieve Analysis 150 μm

Table 23: First sieve analysis of grounded salt - 499.23 g

Upper Limit μm	Lower Limit μm	Gross Mass [g]	Tare weight [g]	Net. Mass [g]	x_i [-]	d_{pi} [-]	$x_i \cdot d_{pi}$ [-]
300	224	334.40	334.4	0.00	0.0000	262	0.0000
224	200	562.31	226.08	336.23	0.6735	212	142.7814
200	140	444.90	334.84	110.06	0.2205	170	37.4781
140	125	359.15	325.4	33.75	0.0676	132.5	8.9575
125	100	224.32	217.91	6.41	0.0128	112.5	1.4445
100	50	359.42	353.97	5.45	0.0109	75	0.8188
50	63	417.10	414.38	2.72	0.0054	56.5	0.3078
63	40	241.81	237.2	4.61	0.0092	51.5	0.4756
40	0	192.50	192.5	0.00	0.0000	20	0.0000
			Σ Net. Mass [g]:	499.23		d_p:	192.26

Table 24: Second sieve analysis of grounded salt - 499.47 g

Upper Limit μm	Lower Limit μm	Gross Mass [g]	Tare weight [g]	Net. Mass [g]	x_i [-]	d_{pi} [-]	$x_i \cdot d_{pi}$ [-]
300	224	334.40	334.4	0.00	0.0000	262	0.0000
224	200	549.36	226.08	323.28	0.6472	212	137.2162
200	140	456.05	334.84	121.21	0.2427	170	41.2551
140	125	355.44	325.4	30.04	0.0601	132.5	7.9690
125	100	225.90	217.91	7.99	0.0160	112.5	1.7997
100	50	360.32	353.97	6.35	0.0127	75	0.9535
50	63	418.66	414.38	4.28	0.0086	56.5	0.4842
63	40	243.52	237.2	6.32	0.0127	51.5	0.6517
40	0	192.50	192.5	0.00	0.0000	20	0.0000
			Σ Net. Mass [g]:	499.47		d_p:	190.33

Table 25: Third sieve analysis of grounded salt - 499.52 g

Upper Limit μm	Lower Limit μm	Gross Mass [g]	Tare weight [g]	Net. Mass [g]	x_i [-]	d_{pi} [-]	$x_i \cdot d_{pi}$ [-]
300	224	334.40	334.4	0.00	0.0000	262	0.0000
224	200	539.20	226.08	313.12	0.6272	212	132.9677
200	140	459.14	334.84	124.30	0.2490	170	42.3272
140	125	361.81	325.4	36.41	0.0729	132.5	9.6635
125	100	223.90	217.91	5.99	0.0120	112.5	1.3498
100	50	363.64	353.97	9.67	0.0194	75	1.4527
50	63	417.72	414.38	3.34	0.0067	56.5	0.3780
63	40	243.89	237.2	6.69	0.0134	51.5	0.6901
40	0	192.50	192.5	0.00	0.0000	20	0.0000
			Σ Net. Mass [g]:	499.52		d_p:	188.83

The d_p of the individual tests were 192.26 µm, 190.33 µm and 188.83 µm.
$d_p = 190$ µm
$d_{sv} = 150$ µm - according to Equation 1 with an assumed form factor (ϕ) of 0.8.

C Results of the Vessel Doser (VD)

Table 26: Data used for Vessel Doser (VD) calculations

Object #	Flow rate [l/min]	Flow rate ratio [-]	Diameter outlet tube [mm]	Mass Flux [g/min]
1	8	0.25	5	11.55
2	8	0.25	9	14.60
3	8	0.75	5	10.04
4	8	0.75	9	14.93
5	20	0.25	5	30.03
6	20	0.25	9	60.47
7	20	0.75	5	23.18
8	20	0.75	9	54.78
9	8	0.25	5	10.29
10	8	0.25	9	18.97
11	8	0.75	5	10.33
12	8	0.75	9	16.85
13	20	0.25	5	28.91
14	20	0.25	9	59.60
15	20	0.75	5	26.70
16	20	0.75	9	58.46
17	8	0.25	5	9.72
18	8	0.25	9	19.30
19	8	0.75	5	9.84
20	8	0.75	9	16.14
21	20	0.25	5	27.19
22	20	0.25	9	52.59
23	20	0.75	5	26.49
24	20	0.75	9	55.15

Table 27: Regression results of the Vessel Doser (VD) - First Approach

Object #	Target Value	Regr. Result	Difference	Cook's D
1	11.55	5.3283	-6.222	$5.206 \cdot 10^{-2}$
2	14.60	23.4592	8.859	$1.056 \cdot 10^{-1}$
3	10.04	3.6342	-6.406	$5.519 \cdot 10^{-2}$
4	14.93	21.7650	6.835	$6.283 \cdot 10^{-2}$
5	30.03	33.7442	3.714	$1.855 \cdot 10^{-2}$
6	60.47	51.8750	-8.595	$9.936 \cdot 10^{-2}$
7	23.18	32.05	8.870	$1.058 \cdot 10^{-1}$
8	54.78	50.1808	-4.599	$2.845 \cdot 10^{-2}$
9	10.29	5.3283	-4.962	$3.311 \cdot 10^{-2}$
10	18.97	23.4592	4.489	$2.710 \cdot 10^{-2}$
11	10.33	3.6342	-6.696	$6.030 \cdot 10^{-2}$
12	16.85	21.7650	4.915	$3.249 \cdot 10^{-2}$
13	28.91	33.7442	4.834	$3.143 \cdot 10^{-2}$
14	59.60	51.8750	-7.725	$8.026 \cdot 10^{-2}$
15	26.70	32.05	5.350	$3.850 \cdot 10^{-2}$
16	58.46	50.1808	-8.279	$9.219 \cdot 10^{-2}$
17	9.720	5.3283	-4.392	$2.594 \cdot 10^{-2}$
18	19.30	23.4592	4.159	$2.327 \cdot 10^{-2}$
19	9.840	3.6342	-6.206	$5.180 \cdot 10^{-2}$
20	16.14	21.7650	5.625	$4.255 \cdot 10^{-2}$
21	27.19	33.7442	6.554	$5.777 \cdot 10^{-2}$
22	52.59	51.8750	-0.715	$6.876 \cdot 10^{-4}$
23	26.49	32.05	5.560	$4.158 \cdot 10^{-2}$
24	55.15	50.1808	-4.969	$3.321 \cdot 10^{-2}$

Table 28: Regression results of the Vessel Doser (VD) - Improved Model

Object #	Target Value	Regr. Result	Difference	Cook's D
1	2.4467	2.3003	-0.1464	$1.202 \cdot 10^{-1}$
2	2.6810	2.9147	0.2337	$3.063 \cdot 10^{-1}$
3	2.3066	2.2308	-0.0758	$3.220 \cdot 10^{-2}$
4	2.7034	2.8452	0.1418	$1.128 \cdot 10^{-1}$
5	3.4022	3.3949	-0.0073	$3.004 \cdot 10^{-4}$
6	4.1022	4.0093	-0.0929	$4.835 \cdot 10^{-2}$
7	3.1433	3.3254	0.1821	$1.859 \cdot 10^{-1}$
8	4.0033	3.9398	-0.0635	$2.264 \cdot 10^{-2}$
9	2.3312	2.3003	-0.0309	$5.344 \cdot 10^{-3}$
10	2.9429	2.9147	-0.0281	$4.440 \cdot 10^{-3}$
11	2.3351	2.2308	-0.1042	$6.095 \cdot 10^{-2}$
12	2.8244	2.8452	0.0209	$2.442 \cdot 10^{-3}$
13	3.3642	3.3949	0.0307	$5.282 \cdot 10^{-3}$
14	4.0877	4.0093	-0.0784	$3.444 \cdot 10^{-2}$
15	3.2847	3.3254	0.0407	$9.295 \cdot 10^{-3}$
16	4.0683	3.9398	-0.1286	$9.268 \cdot 10^{-2}$
17	2.2742	2.3003	0.0261	$3.826 \cdot 10^{-3}$
18	2.9601	2.9147	-0.0454	$1.155 \cdot 10^{-2}$
19	2.2865	2.2308	-0.0557	$1.737 \cdot 10^{-2}$
20	2.7813	2.8452	0.0639	$2.291 \cdot 10^{-2}$
21	3.3029	3.3949	0.0920	$4.750 \cdot 10^{-2}$
22	3.9625	4.0093	0.0468	$1.227 \cdot 10^{-2}$
23	3.2768	3.3254	0.0486	$1.325 \cdot 10^{-2}$
24	4.0101	3.9398	-0.0703	$2.769 \cdot 10^{-2}$

Table 29: Regression results of the Vessel Doser (VD) - Final Approach

Object #	Target Value	Regr. Result	Difference	Cook's D
1	2.4467	2.2656	-0.1811	$1.543 \cdot 10^{-1}$
2	2.6810	2.8799	0.1989	$1.862 \cdot 10^{-1}$
3	2.3066	2.2656	-0.0410	$7.916 \cdot 10^{-3}$
4	2.7034	2.8799	0.1766	$1.467 \cdot 10^{-1}$
5	3.4022	3.3601	-0.0421	$8.326 \cdot 10^{-3}$
6	4.1022	3.9746	-0.1276	$7.660 \cdot 10^{-2}$
7	3.1433	3.3601	0.2168	$2.212 \cdot 10^{-1}$
8	4.0033	3.9745	-0.0288	$3.897 \cdot 10^{-3}$
9	2.3312	2.2656	-0.0656	$2.026 \cdot 10^{-2}$
10	2.9429	2.8799	-0.0629	$1.861 \cdot 10^{-2}$
11	2.3351	2.2656	-0.0695	$2.272 \cdot 10^{-2}$
12	2.8244	2.8799	0.0556	$1.455 \cdot 10^{-2}$
13	3.3642	3.3601	-0.0041	$7.760 \cdot 10^{-5}$
14	4.0877	3.9746	-0.1131	$6.019 \cdot 10^{-2}$
15	3.2847	3.3601	0.0755	$2.679 \cdot 10^{-2}$
16	4.0683	3.9746	-0.0938	$4.139 \cdot 10^{-2}$
17	2.2742	2.2656	-0.0086	$3.505 \cdot 10^{-4}$
18	2.9601	2.8799	-0.0801	$3.021 \cdot 10^{-2}$
19	2.2865	2.2656	-0.0209	$2.055 \cdot 10^{-3}$
20	2.7813	2.8799	0.0987	$4.580 \cdot 10^{-2}$
21	3.3029	3.3601	0.0573	$1.543 \cdot 10^{-2}$
22	3.9626	3.9745	0.0120	$6.792 \cdot 10^{-4}$
23	3.2768	3.3601	0.0834	$3.269 \cdot 10^{-2}$
24	4.0101	3.9746	-0.0355	$5.933 \cdot 10^{-3}$

D Results of the Revolver Doser (RD)

Table 30: Data used for Revolver Doser (RD) calculations

Object #	h [mm]	RPM [1/min]	Mass Flux [g/min]
1	3	13.39	1.34
2	3	13.39	1.30
3	3	13.39	1.42
4	3	5.99	0.72
5	3	5.99	0.73
6	3	5.99	0.77
7	3	1.72	0.43
8	3	1.72	0.42
9	3	1.72	0.44
10	2.13	13.39	0.80
11	2.13	13.39	0.82
12	2.13	13.39	0.77
13	2.13	5.99	0.44
14	2.13	5.99	0.42
15	2.13	5.99	0.45
16	2.13	1.72	0.27
17	2.13	1.72	0.29
18	2.13	1.72	0.28

Table 31: Regression results of the Vessel Doser (RD) - First Approach

Object #	Target Value	Regr. Result	Difference	Cook's D
1	1.34	1.2362	-0.1038	$1.264 \cdot 10^{-1}$
2	1.30	1.2362	-0.0638	$4.779 \cdot 10^{-2}$
3	1.42	1.2362	-0.1838	$3.963 \cdot 10^{-1}$
4	0.72	0.7763	0.0563	$1.625 \cdot 10^{-2}$
5	0.73	0.7763	0.0463	$1.098 \cdot 10^{-2}$
6	0.77	0.7763	0.0063	$2.018 \cdot 10^{-4}$
7	0.43	0.5109	0.0809	$6.140 \cdot 10^{-2}$
8	0.42	0.5109	0.0909	$7.752 \cdot 10^{-2}$
9	0.44	0.5109	0.0709	$4.716 \cdot 10^{-2}$
10	0.80	0.8995	0.0995	$1.161 \cdot 10^{-1}$
11	0.82	0.8995	0.0795	$7.410 \cdot 10^{-2}$
12	0.77	0.8995	0.1295	$1.966 \cdot 10^{-1}$
13	0.44	0.4396	-0.0004	$8.038 \cdot 10^{-7}$
14	0.42	0.4396	0.0196	$1.972 \cdot 10^{-3}$
15	0.45	0.4396	-0.0104	$5.545 \cdot 10^{-4}$
16	0.27	0.1742	-0.0958	$8.603 \cdot 10^{-2}$
17	0.29	0.1742	-0.1158	$1.257 \cdot 10^{-1}$
18	0.28	0.1742	-0.1058	$1.049 \cdot 10^{-1}$

Table 32: Regression results of the Vessel Doser (RD) - Final Approach

Object #	Target Value	Regr. Result	Difference	Cook's D
1	0.2927	0.3092	0.0165	$3.799 \cdot 10^{-3}$
2	0.2623	0.3092	0.0468	$3.058 \cdot 10^{-2}$
3	0.3507	0.3092	-0.0415	$2.403 \cdot 10^{-2}$
4	-0.3285	-0.3782	-0.0497	$1.507 \cdot 10^{-2}$
5	-0.3147	-0.3782	-0.0635	$2.460 \cdot 10^{-2}$
6	-0.2614	-0.3782	-0.1168	$8.334 \cdot 10^{-2}$
7	-0.8439	-0.7748	0.0692	$5.347 \cdot 10^{-2}$
8	-0.8675	-0.7748	0.0927	$9.603 \cdot 10^{-2}$
9	-0.8209	-0.7748	0.0462	$2.384 \cdot 10^{-2}$
10	-0.2231	-0.1686	0.0545	$4.150 \cdot 10^{-2}$
11	-0.1985	-0.1686	0.0298	$1.242 \cdot 10^{-2}$
12	-0.2614	-0.1686	0.0927	$1.201 \cdot 10^{-1}$
13	-0.7134	-0.8559	-0.1426	$1.242 \cdot 10^{-1}$
14	-0.8675	-0.8559	0.0115	$8.141 \cdot 10^{-4}$
15	-0.6733	-0.8559	-0.1826	$2.037 \cdot 10^{-1}$
16	-0.1309	-0.1253	0.0568	$3.599 \cdot 10^{-2}$
17	-0.1238	-0.1253	-0.0147	$2.411 \cdot 10^{-3}$
18	-0.1347	-0.1253	0.0945	$9.976 \cdot 10^{-2}$

References

[1] R. Remus, MA. Aguado-Monsonet, and S. Roudier. *Best available techniques (BAT) reference document for iron and steel production.* European Commission Joint Research Centre Institute for Prospective Technological Studies, 2010. doi: 10.2791/97469.

[2] B. Metz, O. Davidson, H.C. de Coninck, M. Loos, and L.A. Meyer. *Carbon dioxide Capture and Storage.* Cambridge University, 2005.

[3] D. Ameling. 8 th intern. arab iron and steel conf. In *Steel - Innovative solutions for energy and resource challenges*, 2008.

[4] M. Harasek, C. Maier, C. Jordan, M. Bösenhofer, and C. Feilmayr. Investigation of alternative reducing agent conversion in the raceway cavity of blast furnaces by numerical simulation. In *AISTech 2016 Proceedings*, 2016. doi: 10.3303/CET1335224.

[5] Y. Zhuo and Y. Shen. Three-dimensional transient modelling of coal and coke co-combustion in the dynamic raceway of ironmaking blast furnaces. *Applied Energy*, 261:1–14, 2020. doi: https://doi.org/10.1016/j.apenergy.2019.114456.

[6] A. Babich, D. Senk, and S. Born. Interaction between co-injected substances with pulverized coal into the blast furnace. *ISIJ International*, 54(12):2704–2712, 2014. doi: 10.2355/isijinternational.54.2704.

[7] M. Bösenhofer, E. Wartha, C. Jordan, C. Feilmayr, H. Stocker, F. Hauzenberger, Johannes Rieger, Stefan Tjaden, Arleen Walk, and Michael Harasek. Suitability of pulverised coal testing facilities for blast furnace applications. *Ironmaking & Steelmaking*, pages 1–12, Jan 2019. doi: 10.1080/03019233.2019.1565152.

[8] Y. Tomita J. Hong, Y. Shen. Phase diagrams in dense phase pneumatic transport. *Powder Technology*, 84:213–219, 1995. doi: 10.1016/0032-5910(95)02996-F.

[9] H. Kalman E. Rabinovich. Flow regime diagram for vertical pneumatic conveying and fluidized bed systems. *Powder Technology*, 207:119–133, 2011. doi: 10.1016/j.powtec.2010.10.017.

[10] D. Wang and L.-S. Fan. Particle characterization and behavior relevant to fluidized bed combustion and gasification systems. *Fluidized Bed Technologies for Near-Zero Emission Combustion and Gasification*, pages 42–76, 12 2013. doi: 10.1533/9780857098801.1.42.

[11] H. G. Merkus. *Particle Size Measurements: Fundamentals, Practice, Quality*. Springer Science and Business Media, 2009.

[12] D. Geldart. Types of gas fluidization. *Powder technology*, 7:285–292, 1973. doi: 10.1016/0032-5910(73)80037-3.

[13] C.Y. Wen and Y.H. Yu. A generalized method for predicting the minimum fluidization velocity. *AIChE J.*, 12:610–612, 1966. doi: 10.1002/aic.690120343.

[14] HG. Wypych. *Handbook of Solvents, Volume 2 - Use, Health, and Environment*. ChemTec Publishing, 2019.

[15] P.C. Carman. Fluid flow through granular beds. *Transactions, Institution of Chemical Engineers*, 15:150–166, 1937. doi: 10.1016/S0263-8762(97)80003-2.

[16] S. Ergun. Fluid flow through packed columns. *Chem. Eng. Prog.*, 48: 89–94, 1952.

[17] H. Hofbauer. *Wirbelschichttechnik*. Technische Universität Wien, March 2019.

[18] T. Tsuji, E. Narita, and T. Tanaka. Effect of a wall on flow with dense particles. *Advanced Powder Technology*, pages 565–574, 2013. doi: 10.1016/j.apt.2012.11.006.

[19] J.R. Grace H.T. Bi. Flow regime diagrams for gas-solid fluidization and upward transport. *International Journal of Multiphase Flow*, 2: 1229–1236, 1995. doi: 10.1016/0301-9322(95)00037-X.

[20] K. Siebertz, D. Van Bebber, and T. Hochkirchen. *Statistische Versuchsplanung - Design of Experiments (DoE)*. Springer, 2010.

[21] J. Cohen, P. Cohen, S.G. West, and L.S. Aiken. *Applied multiple regression/correlation analysis for the behavioral sciences*. Lawrence Erlbaum Associates, 2003.

[22] R. M. O'brien. A caution regarding rules of thumb for variance inflation factors. *Quality & Quantity*, 41(5):673–690, Mar 2007. doi: 10.1007/s11135-006-9018-6.

[23] C. M. Judd, G. H. McClelland, and C. S. Ryan. *Data Analysis: A Model Comparison Approach To Regression, ANOVA, and Beyond*. Taylor and Francis Ltd, 2017.

[24] J. Kirsch. Pneumatic injection of solids intopyrometallurgical processes:past, present, and future. In *Southern African Pyrometallurgy*, pages 371–384, 2006.

[25] S. Puttinger, G. Holzinger, and S. Pirker. Investigation of highly laden particle jet dispersion by the use of a high-speed camera and parameter-independent image analysis. *Powder Technology*, 234:46–57, Jan 2013. doi: 10.1016/j.powtec.2012.09.034.

[26] C. Liang, P. Xu, G. Xu, X. Chen, C. Zhao, and L. Duan. Comparison on flow characteristics of dense-phase pneumatic conveying of biomass powder and pulverized coal at high pressure. *Energy Sources, Part A: Recovery, Utilization, and Environmental Effects*, 37:583–589, Feb 2015. doi: 10.1080/15567036.2011.585384.

[27] N. Vorobiev. *Optische Untersuchung des Abbrandverhaltens von Brennstoffpartikeln in Oxyfuel-Atmosphäre*. Fakultät für Maschinenbau der Ruhr-Universität Bochum, 2020.

[28] K. Park K. H. Henthorn and J. S. Curtis. Measurement and prediction of pressure drop in pneumatic conveying: Effect of particle characteristics, mass loading, and reynolds number. *Ind. Eng. Chem. Res.*, pages 5090–5098, 2005. doi: 10.1021/ie049505e.

[29] Madison A. Kelley, Micah S. Jakulewicz, Christopher B. Dreyer, Terence E. Parker, and Jason M. Porter. System overview and characterization of a high-temperature, high-pressure, entrained-flow, laboratory-scale gasifier. *Review of Scientific Instruments*, 86:1–8, May 2015. doi: 10.1063/1.4921196.

[30] J. Köser, L. G. Becker, N. Vorobiev, M. Schiemann, V. Scherer, B. Böhm, and A. Dreizler. Characterization of single coal particle combustion within oxygen-enriched environments using high-speed OH-PLIF. *Applied Physics B*, 121(4):459–464, Oct 2015. doi: 10.1007/s00340-015-6253-3.